# REPORT DOCUMENTATION PAGE

| 1. REPORT DATE *(DD-MM-YYYY)* | 2. REPORT TYPE | 3. DATES COVERED *(From - To)* |
|---|---|---|

**4. TITLE AND SUBTITLE**

5a. CONTRACT NUMBER

5b. GRANT NUMBER

5c. PROGRAM ELEMENT NUMBER

**6. AUTHOR(S)**

5d. PROJECT NUMBER

5e. TASK NUMBER

5f. WORK UNIT NUMBER

**7. PERFORMING ORGANIZATION NAME(S) AND ADDRESS(ES)**

**8. PERFORMING ORGANIZATION REPORT NUMBER**

**9. SPONSORING / MONITORING AGENCY NAME(S) AND ADDRESS(ES)**

**10. SPONSOR/MONITOR'S ACRONYM(S)**

**11. SPONSOR/MONITOR'S REPORT NUMBER(S)**

**12. DISTRIBUTION / AVAILABILITY STATEMENT**

**13. SUPPLEMENTARY NOTES**

**14. ABSTRACT**

**15. SUBJECT TERMS**

| 16. SECURITY CLASSIFICATION OF: | | | 17. LIMITATION OF ABSTRACT | 18. NUMBER OF PAGES | 19a. NAME OF RESPONSIBLE PERSON |
|---|---|---|---|---|---|
| a. REPORT | b. ABSTRACT | c. THIS PAGE | | | 19b. TELEPHONE NUMBER *(include area code)* |

# DEMONSTRATION OF A WINGLESS ELECTROMAGNETIC AIR VEHICLE
## Applied Physics Research Group, University of Florida, Gainesville

**PI: Subrata Roy, Co-PIs: David Arnold, Jenshan Lin, Tony Schmidt and Rick Lind**

Students: Ryan Durscher, Mark Riherd, Tomas Houba, Richard Anderson, Justin Zito, Joaquin Casanova, Carlton Thompson, Daniel Blood, Dong Tran

Recent advances in materials, plasma discharges and power source allows us to take a revolutionary leap in unmanned air vehicle systems. We propose a patented[*] Wingless Electromagnetic Air Vehicle (WEAV), which employs no moving parts and assures near instantaneous response time. **For the first time,** the aircraft structure, propulsion, energy production and storage, and control will be combined in an integrated system. Such systems will be invaluable in close air support missions by providing situational awareness and damage assessment in a complex and chaotic battlefield environment. If necessary, the vehicle will also be designed to deliver focused and calibrated firepower. It will support AFRL strategic vision of 2015-2030 to "deliver precision effects: ubiquitous, swarming sensors and shooters" and will be relevant to the WMD sensing ISR missions.

With a flight profile similar to a spinning disk, WEAV will be able to soar for long periods of time and utilize EHD thrust to acquire and maintain desired altitude and attitude. This revolutionary concept is based on the use of an electro-(or magneto) hydrodynamic (EHD/MHD) thrust generation surface that is coated with multiple layers of dielectric polymers with exposed and/or embedded electrodes for propulsion and dynamic control. This technology has the unique capability of imparting an accurate amount of thrust into the surrounding fluid enabling the vehicle to move and react. Thrust is instantaneously and accurately controlled by the applied power, its waveform, duty cycle, phase lag and other electrical parameters. Once the applied power is removed the thrust vanishes. Combining the EHD/MHD technology with emerging batteries and thin-film photovoltaics provides both energy source and storage in the same structure.

> *The goal of this project is the proof-of-concept demonstration of an electromagnetically driven wingless aircraft\* with no moving component that will be able to self-lift, hover and fly reliably especially under gust and impact conditions.*

The proposed wingless design will overcome the main deficiencies of traditional rotary or wing-based vehicles. First, WEAV will require significantly lower hover power requirements. Second, since there are no rotating components, the problem of turbulent signature is minimized. Third, even under anticipated gust conditions, the operational physics ensures a mechanism for lift generation, directed motion and accurate control. Finally, the design principles naturally safeguard operational reliability, flight stability and bump resistance.

This initial (proof-of-concept) phase 1 of this work were performed by a team of scientists from the University of Florida. This phase involved building, characterization, testing, and simulation of plasma actuators, aerodynamics, power and propulsion systems, micromachining and microfabrication. A simple cylindrical geometry was considered for lifting using plasma force in atmospheric condition. This effort also leveraged recent discoveries made with AFOSR grant investments to the investigators. The following five sections describe our achievements and challenges: I. Target matrices. II. Experiments with novel plasma actuators and plasma propulsion. III. Numerical modeling of various cylindrical wingless geometries for aerodynamics and flight dynamics. IV. Novel power supply unit – circuit, simulation and testing. V. Fabrication of these devices. VI. Experimental data collection and numerical modeling of a plasma tunnel.

## I. Target Matrices.

The initial proof-of-concept phase was divided into two segments: Phase 1a and Phase 1b.

**A. Initial targets at the beginning of Phase 1a**

---

[*] Roy, S. "Wingless Hovering of Micro Air Vehicle (WHOMAV)," Patent EP2046640 Granted on Oct 12, 2011, first Publication WO 2008/016928, filed in May 2006, filed for National Phase in the US, EPO, China and Japan.

When we started the project Phase 1a, we intended to demonstrate the theory and WEAV concept by the following Target (Go-No Go) Matrix.

*Target Matrix*

|  | State-of-the-art | Phase 1a goal | Phase 1b goal |
|---|---|---|---|
| **Thrust** | 0.02 gm/m | 1gm/m | 10gm/m |
| **Power at supply** | 80-100 w | 15-25 w | 5 w |
| **Lift-off** | N/A | Circular thin shape with external supply | WEAV design with onboard supply |

**B. Revised targets at the beginning of Phase 1b**

|  | State-of-the-art | Phase 1a goal | Achievement | Phase 1b goal | Phase 2 goal |
|---|---|---|---|---|---|
| **Thrust** | 0.2 gm/m | 1gm/m | (>3gm/m) | >10gm/m (achieved 12 gm/m) | • >100 gm/m |
| **Power** | 80-100 w | 15-25 w | (<14 w) | <5 w | Reasonable power |
| **Lift-off** | N/A | Circular thin plate with external power supply | (> 2 min hovering) | • Lift off from chicken wire mesh table 3 ft above floor. Hover > 5 min at 1 ft above table (4 ft above floor).<br>• L/W > 1.2 | • Operational WEAV design with Payload.<br>• Alt – 0 to 500 ft AGL<br>• Flight time > 1 hr |
| **DBD Wind Tunnel** | N/A | N/A |  | • Tunnel < 1 ft long<br>• Measured air velocity at bottom of outlet > 3 m/s.<br>• Pressure differential between inlet and outlet is sufficient to enable flight demo L/W > 1.2 when also including thrust generated by the plasma actuators. | • N/A |
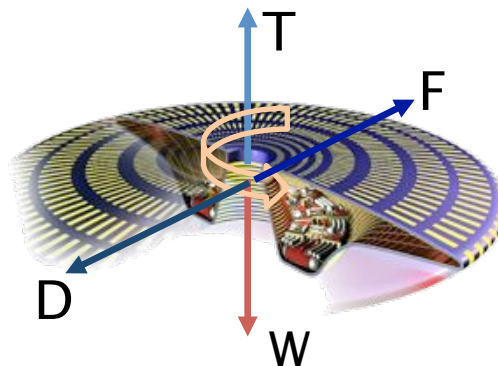
To date our progress can be summarized in the following chart of generated thrust (T) over WEAV weight (W).
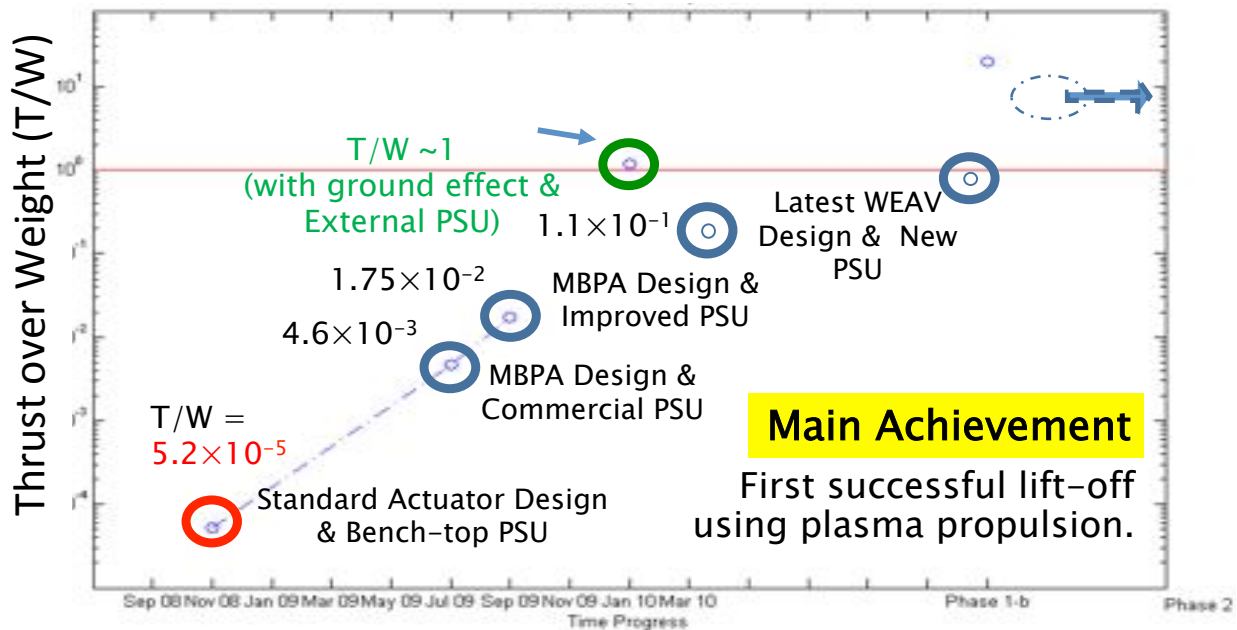


We have made nearly four orders of magnitude improvement of T/W in the past two an[...] However, there are plenty of remaining challenges. The proposed WEAV vehicle wi[...] mo[...] uo[...] ature), wingless surface. The electromagnetic force in WEAV is generated by [...] u[...] at[...] oltage between a set of grounded and powered electrodes separated by a polymer insulator [...] po[...] applied magnetic field. It will generate a vertical fluid column induced by a polyphase power supply in the central hollow section to create sufficient upward or downward force for lift-off, hover or landing. The outer surface as well as the inner conical surface will facilitate maneuverability of the craft. The aerodynamic concept anchors on plasma-based Lorentz Force induced circulation control that enhances flight stability. Initial estimates show that the nominal cruise speed of the wingless design will be about 4-10m/s (12-33 ft/s).

There are four major advantages of the proposed revolutionary concept over its winged counterparts. **First**, internal surfaces (say for a donut shape) used for thrust generation are less affected by the unsteadiness of the surrounding flow. **Second**, rapid response of the plasma force and absence of any moving part assures excellent aerodynamic reliability to adequately manage massive, time-dependent separation which will otherwise stall traditional wings or copter blades. **Third**, the wind load on an annular disc in neutral equilibrium is at a minimum. There is a need to have feedback control to comply with wind load for maximum stability. **Fourth**, its circular design allows it to have a full 360 degree maneuverability.

This concept is based on sound physical principles. Its successful operation will hinge on long term research and development commitment.

## II.   Experiments with novel plasma actuators and plasma propulsion.

### A. Thruster Designs
#### 1. *Multi-Barrier Actuators*

The multi-barrier plasma actuator[1] (MBPA) is an extension on the conventional single layer dielectric barrier discharge (DBD) design. The MPBA has additional dielectric layers and powered electrodes kept at phase differences in an effort to improve thrust production (figure 1). To evaluate the performance of these devices both bi-layer and tri-layer devices were tested and compared with a standard single layer configuration. The bi-layer designs consisted of three electrodes with the middle/second electrode grounded. The tri-layer configurations tested

(as illustrated in figure 1) had four electrodes, each supplied with a 60° phase lag relative to the electrode above it
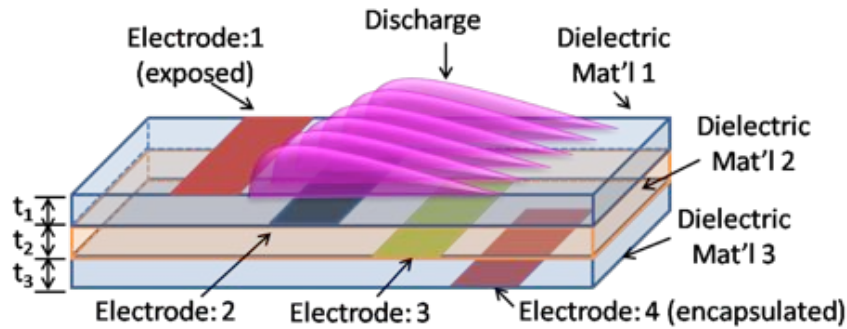


**Figure 1. Tri-layer multi-barrier plasma actuator (MBPA) schematic.**

Sample result for the MBPA trials are shown in figure 2. As shown in figure 2a for constant overall actuator thickness the standard actuator results in the largest thrust production for a given voltage up to its saturation point. The bi-layer MBPA was able to reproduce the same forces however it was necessary to operate at a higher input potential. The force to consumed power ratio, denoted as the actuator effectiveness in figure 2b, was drastically impacted by the MBPA design, and in particular in the bi-layer configuration. A ~40% increase in effectiveness was observed between the bi-layer MBPA and standard actuator, thus making the MBPA configuration a more efficient design. The tri-layer design showed the least amount of promise based on either merit (force or effectiveness). The increase in effectiveness of the bi-layer configuration is currently attributed to the lack of patristic discharge that occurs on the standard actuator due to the potential being concentrated on a single electrode.
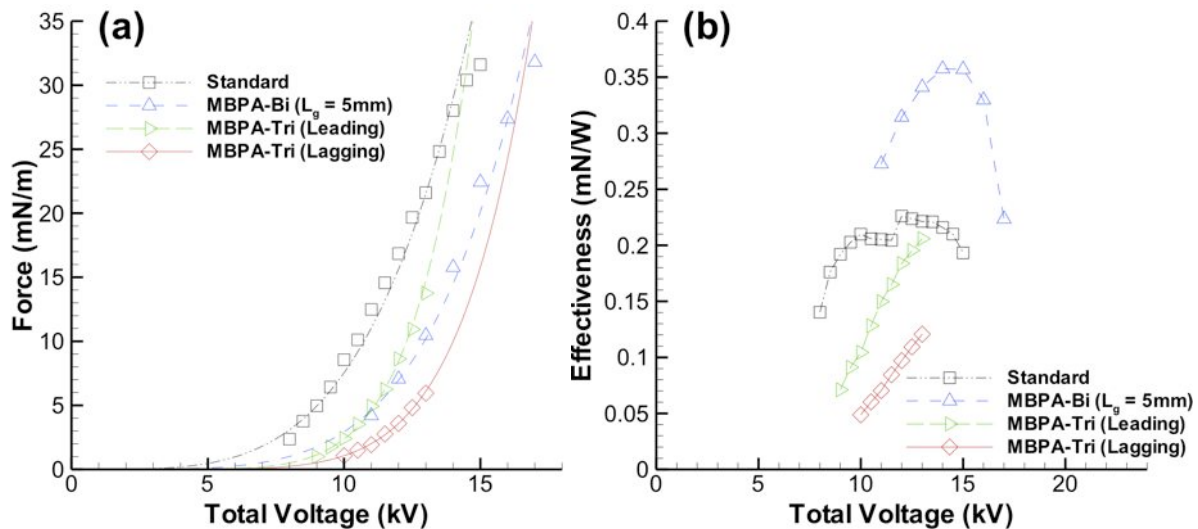


**Figure 2. Comparison of actuator configurations: a) force and b) effectiveness.**

The influence or importance of the middle grounded electrode in the bi-layer design was also investigated. It was found that the middle electrode played no significant role in terms of both force production (figure 3) and total power consumption (figure 4). It did, however, have an influence on the power distribution supplied to the two (upper and lower) electrodes. When the middle electrode was present, the upper (exposed) electrode consumed significantly more power than the lower (encapsulated) electrode. In this case the majority of the total power consumed by the device was supplied to the exposed electrode. Conversely, when the middle electrode was removed, the consumed power between the upper and lower electrodes was approximately equal. These results would have a significant effect on the design of the power supply for this type of actuator.
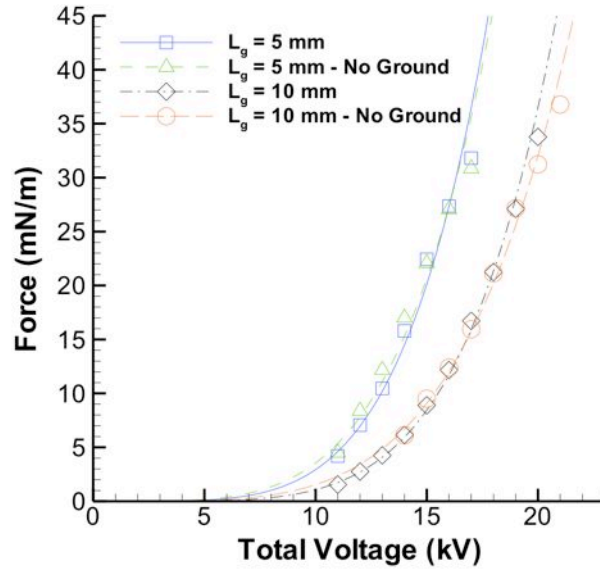
**Figure 3. Influence of the grounded electrode in the bi-layer MBPA configuration on force production.**
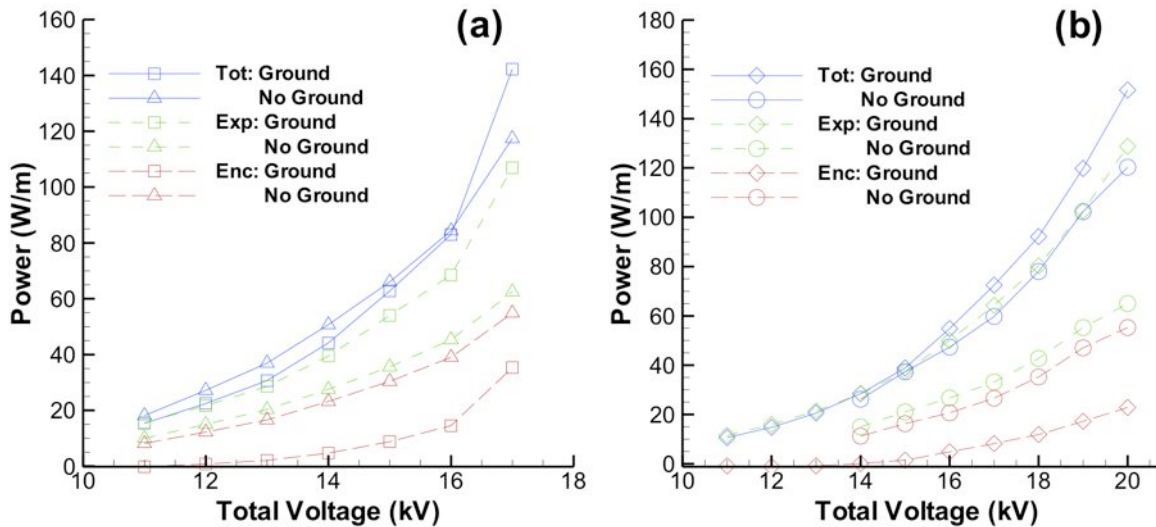$L_g$ **represents the total gap between the upper and lower electrodes**



**Figure 4.  Power distribution in a bi-layer MBPA with and without a middle grounded electrode present.**
**a) $L_g$ = 5 mm and b) $L_g$ = 10 mm. $L_g$ represents the total gap between the upper and lower electrodes**

2.  *Serpentine Actuators*

    Unlike the standard linear DBD actuator, the serpentine design[2] provides a fully three-dimensional flow control mechanism that combines the effects of a linear actuator and a plasma synthetic jet[3].  Intuitively, as one moves along the span of the actuator, there is a spreading of the fluid at the crest while there is a pinching in the trough (figure 5). Such a configuration introduces a vectoring of the fluid that could be potentially beneficial on various surfaces of the WEAV design.
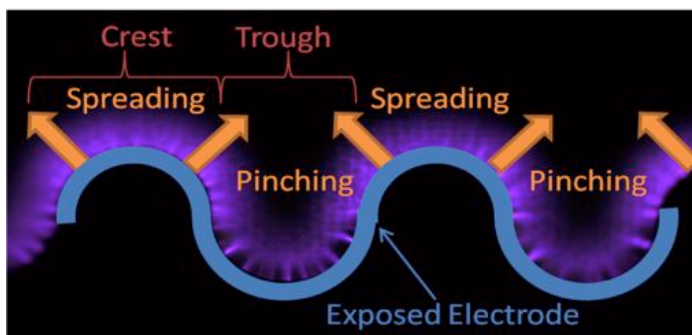
**Figure 5. Circular serpentine plasma actuator.**[4]

As a simple first step in qualitatively determining the influence of a serpentine actuator operating in quiescent air, a laser sheet was positioned as to illuminate the spanwise plane cutting through the trough of actuator. An incense stick was placed near the exposed electrode, the actuator was turned on, and the image was captured using a Nikon D90 SLR camera to provide visual observation of the flow field. The result of this rudimentary test indicated that there was a pinching of the fluid along the plane due to the curved geometry of the electrode. This resulted in the fluid being pushed away from the surface at a ~43° angle (figure 6a). As a comparison, similar flow visualization was performed with a standard linear actuator (figure 6b). The convecting flow was found to create a ~12° angle with the surface; the serpentine configuration provides significantly increased three-dimensional flow effects.
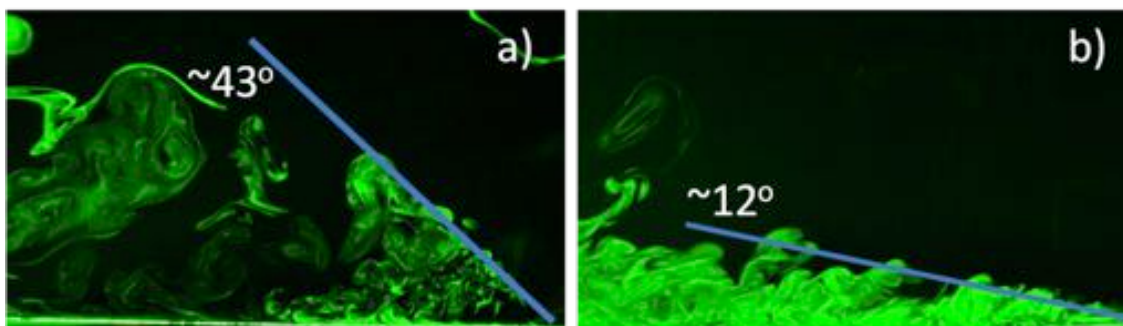


**Figure 6. Instantaneous smoke flow visualization: a) Circular patterned serpentine actuator (plane taken along the trough) and b) standard linear actuator.**

Stereo-particle image velocimetry was later carried out on both circular and rectangular versions of the serpentine design. Both designs were found to influence the fluid in a similar manner. Near the tough (figure 7a) of the actuators the impinging fluid was vectored away from the surface, while at the crests (figure 7b) the fluid was created a near wall jet (reminiscent of the linear DBD). As a result both spanwise as well as streamwise vorticity was generated. This distinctive combination resulted in a unique structure in the induced flow field for the serpentine configurations. As shown by the streamtraces in figures 7c and 7d the fluid follows a corkscrew-like path as it is entrained in the troughs of the actuator. The vectored pinching of the fluid in this region pushes the fluid forward and away from the surface as the z-component of velocity imparts a spin on its path. The fluid at the crest of the actuator is simply pushed forward.
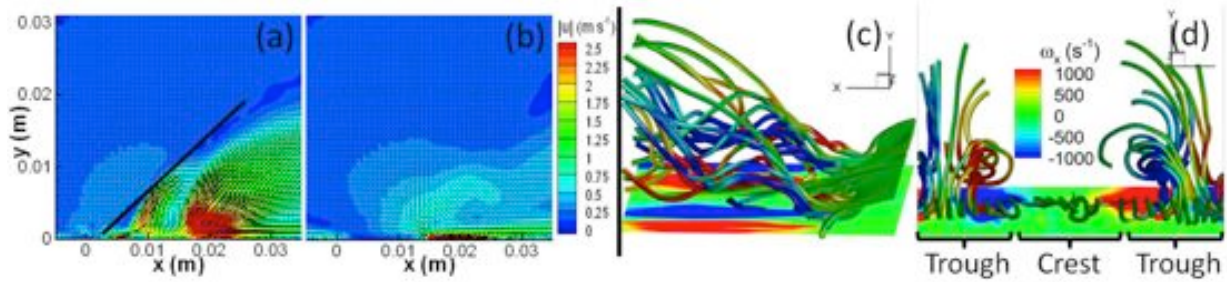
**Figure 7.  Time averaged velocity magnitude (m s$^{-1}$) contours overlaid with x and y-velocity vectors at the trough (a) and crest (b) planes along a rectangular serpentine actuator (14 kVpp). The black solid line indicates the impingement angle in the flow, 38$^{\circ}$. Streamtraces (c,d) colored by $\omega_x$ (s$^{-1}$) showing a corkscrew like structure in the induced flow field..**

3. *Micro-scale Actuators*

   Numerical simulations[5] suggest that shrinking the gap between plasma actuator electrodes increases the electric force density (N/m$^3$) in the discharge region. In addition, with reduced gap the voltage required for plasma discharge is also decreased, in turn leading to physically smaller and lighter power supplies.  Reducing the size and mass of power components is of great importance for flight vehicles.  For these motivations, we began development of microscale plasma actuators, where the electrode and gap dimensions are sub-millimeter (figure 8).  It is envisioned that large arrays of microscale actuators may be connected together to realize macroscopic flow control.
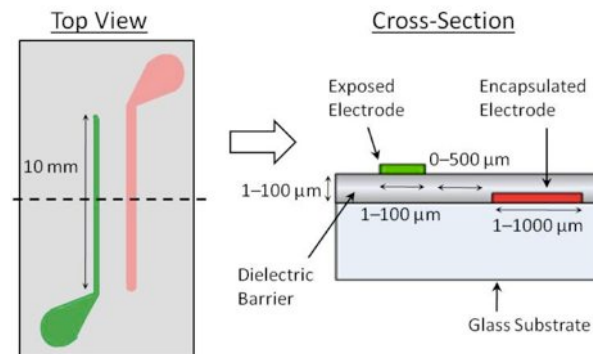


**Figure 8. Top view and cross-section schematics of microscale DBD plasma actuator.**

   Microscale DBD plasma actuators were fabricated in-house[7] at UF's Nanoscience Research Facility (NRF) using wafer-level batch-microfabrication techniques, similar to those used in semiconductor manufacturing.  The devices were fabricated on glass substrates using titanium electrodes and a polyimide dielectric barrier. Glass was used as the substrate to avoid omnidirectional discharge that resulted when using a silicon substrate (due to the semiconducting properties of silicon).   Batch processing allows for high-throughput parallel manufacturing of numerous devices with complex electrode shapes and good dimensional control.  For the preliminary study here, the electrode widths range from 10 µm to 1 mm, and each electrode was 10 mm long (spanwise), as shown in figure 8. The electrodes were 1 µm thick, and the lateral gap between the electrodes ranged from 10 – 500 µm. The polyimide dielectric was ~10 µm thick. Polyimide was chosen for its good metal adhesion and its common use as a dielectric in macroscale DBD plasma devices.  Both single devices and parallel-connected devices were fabricated (figure 9).
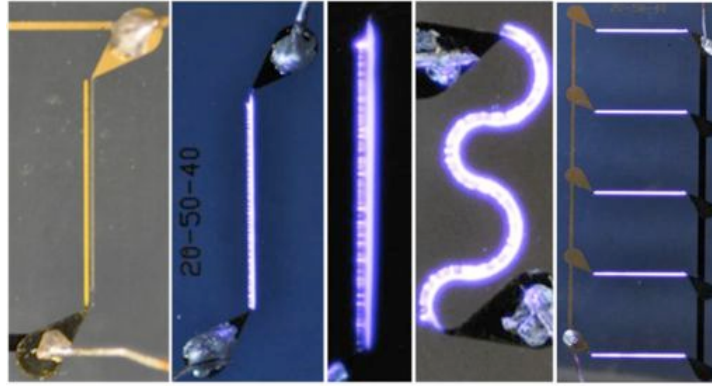
**Figure 9.. Initially fabricated microscale plasma actuators; showing linear, serpentine and arrays of DBD actuators.[7]**

Actuators were characterized for electrical, fluidic and mechanical performance.  For electrical measurements, the voltage across and current flowing into the device terminals were monitored using electrical probes, and a digital oscilloscope was used to simultaneously capture both waveforms.  Typical voltage and current waveforms during plasma discharge are shown in figure 10.  The average power consumed by the actuator is computed by using these voltage and current waveforms, according to

$$P_{avg} = \frac{1}{N} \sum_{i=1}^{N} V_i I_i$$

(1)

where N is the number of samples recorded for each waveform.
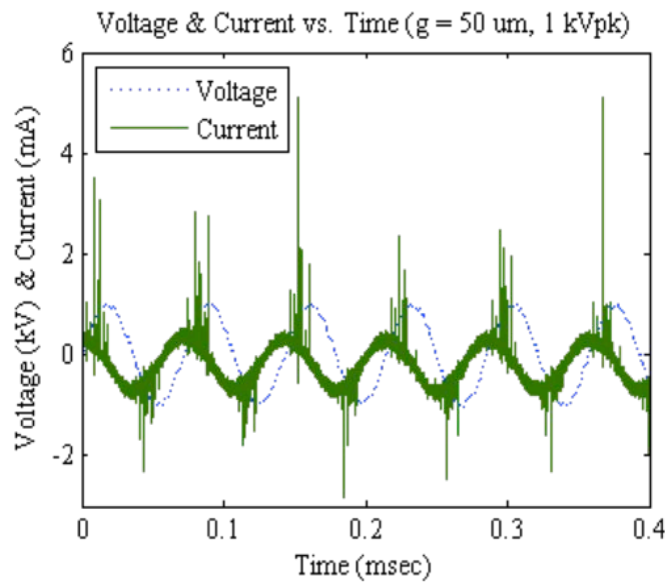


**Figure 10.  Typical voltage and current waveforms during plasma discharge.**

Figure 11 reveals the power consumed for microscale DBD devices with varying electrode widths operated with sinusoidal input at 1 kHz.  Specifically the power per unit electrode length is plotted as a function of peak-to-peak voltage amplitude.  The data in figure 11 is fit with a power-law curve to examine the dependency of power on the

applied voltage. The fit lines indicate the power scales exponentially with the voltage, with the exponent ranging from 3.1 to 3.5 in these data. This matches close with the exponential dependency observed for macroscale actuators for thin dielectrics, shown by Enloe[6] with $P \propto V_{ac}^{7/2}$. The average power consumed (per unit length of electrode) reaches 20 W/m at 5 $kV_{pp}$ and 1 kHz. In contrast, macroscale plasma devices often consume over 100 W/m or more at 25 kVpp (depending on geometry and frequency of operation). The microscale devices offer a substantial reduction in the power requirement; about an order of magnitude in this case.
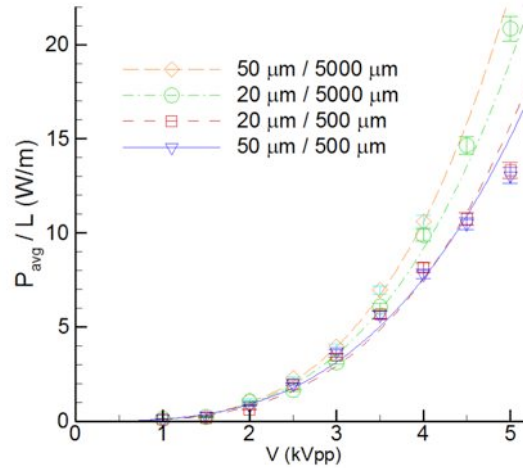


**Figure 11. Average normalized power consumed for four microscale DBD device geometries plotted against applied voltage. The frequency is held constant at 1 kHz in all cases. The nomenclature indicates the width of the powered / grounded electrode, respectively.**

Velocity measurements were made using PIV techniques with a macro lens for a zoomed-in field of view. The actuators were operated at 5 kVpp and 1 kHz. Surprisingly, the microscale DBD actuators produce a velocity flow on the order of that induced from macro DBD devices (1-10 m/s range). Figure 12 compares devices with equal exposed electrodes (10 μm width), but having different ground electrode widths. The ground electrode widths are 1 and 5 mm in figures A and B, respectively. Results reveal the induced velocity reaches ~2.0 m/s in both cases; furthermore, the device with the larger ground extends the downstream length over which the region of greater velocities occurs. This may be attributed to the increase in power consumption for devices with wider ground electrodes (which can be observed in figure 11 above). The profile of the flow grows thicker downstream for the data using a wider ground electrode. This could lead to increased momentum transfer to the fluid. Comparing with macro DBD actuators, which produce flow velocities typically between 3- 8 m/s, the microscale DBD actuators provide similar velocities (upward of 2 m/s) while consuming a 10x reduction in the power requirement.

For mechanical characterization, the reaction force on the device, or equivalently, the device thrust is of interest. A control volume analysis is performed on the velocity flow field using PIV data to extract the device thrust. This analysis follows that used by other groups[8,9] and has shown reasonably good agreement with direct force measurements. The horizontal force component was computed on the order of 1 mN/m (milli-Newton per meter of electrode). Comparing to macro DBD actuators, which produce upwards of 50 mN/m, the microscale actuators cannot provide similar thrust (per single actuator).

Although microscale DBD actuators show promising performance results, especially considering their reduced power requirement and device footprint, they do not provide the thrust or lift that their macro counterparts can provide. In the application at hand, devices are sought to provide the maximum possible thrust for liftoff. For this primary reason, the microscale actuators were not considered as the best thruster geometry and continuing efforts on the actuator design focused on macro DBD actuators.
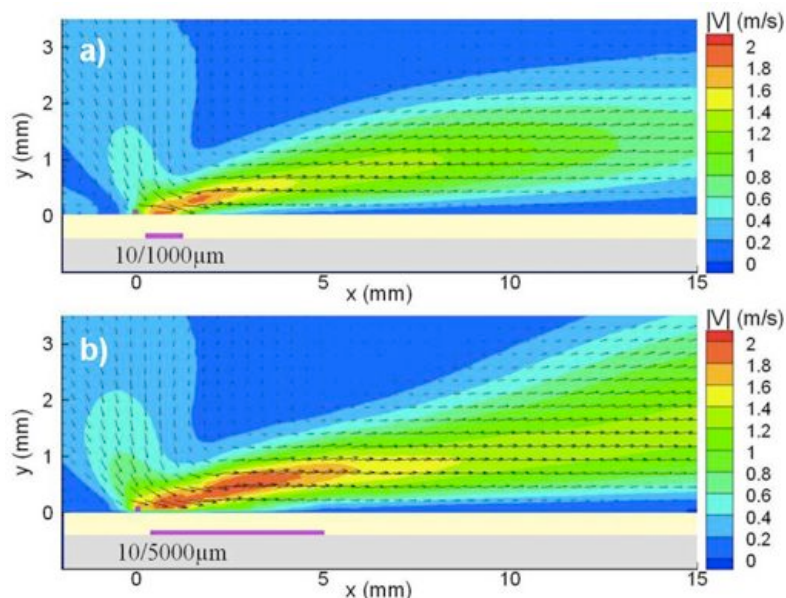
**Figure 12. PIV data comparing devices with (a) 1 mm and (b) 5 mm wide ground electrodes; the wider ground electrode extends the downstream length where the discharge induces the greatest velocities. Both devices have a 10 µm wide powered electrode and have a 100 µm gap between electrodes.**

   Ongoing efforts continually aim to understand the failure mechanisms and make design changes to improve actuator reliability and repeatability. The microscale devices typically last less than five minutes before failure. Concentrated electric field points are the primary cause of failure, causing the dielectric to breakdown near the tips of the powered electrode (figure 13). Sputtering (and subsequent re-deposition) of the electrodes due to plasma/ion bombardment causes erosion and also contributes to device failure. To increase device longevity, high-quality/high-resolution photomasks may be used during the fabrication process enabling features as small as 1 µm.
In addition, other dielectric materials such as polymers (PDMS, PMMA, SU-8), ceramics ($SiO_2$, $Si_3N_4$, SiC, $Al_2O_3$) and semiconductors such as silicon are to be experimented with to determine their effectiveness as the dielectric barrier layer. Combinations of dielectric materials can be used to take advantage of the beneficial material properties of different insulation materials. There are numerous geometric configurations and materials to further investigate for the optimization of microscale DBD plasma actuators.
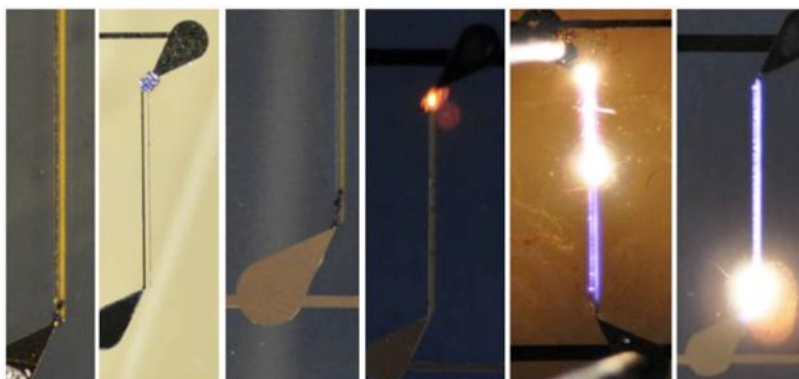


**Figure 13. Deices after failure (leftmost three), and devices at the onset of failure (rightmost three).**

4. *Lorentzian Force Enhancement through Permanent Magnets*

A study was conducted to experimentally evaluate the influence of magnetic fields on DBD plasma discharges. The electrohydrodynamic (EHD) body force acting on the fluid is dependent on the Lorentz force acting on ionized gaseous particles. The force is given by equation 2, where $q$ is the charge (C), $E$ is the electric field (V/m), $v$ is the velocity of the charged particle (m/s), and $B$ is the magnetic flux density (T). In the conventional design configuration, the DBD actuator only utilizes the electric field while the potential magnetic contribution goes unexploited. However, using externally applied magnetic fields, the magnetic contribution ($q$ ($v \times B$)) may be increased, such that its contribution to the overall body force is significant. Furthermore, since Lorentz forces also act on electrons in the plasma, the application of a magnetic field causes the electrons to move in a curved or spiral trajectory as they accelerate towards the electrode. This spiraling can increase the likelihood of electron-molecular collisions, resulting in a higher ionization fraction (i.e. increase the number ionized particles) and hence larger net EHD forces. These initial tests were carried out using external magnetic sources, though if successful, efforts would have been made to embed micro-permanent magnets into the dielectric substrate (figure 14a).

$$\vec{f} = q\left(\vec{E} + \vec{v} \times \vec{B}\right) \tag{2}$$

The influence of magnetic fields was studying by measuring the thrust from a DBD actuator in the presence of magnetic fields from both bar-type permanent magnets and current-carrying coils. The permanent magnet used was an NdFeB (neodymium iron boron) alloy, with a remnant field up to 1.3 T, although the field acting on the actuator is estimated on the order of 100 mT. The magnet was mounted near the actuator (figure 14b) in different configurations; however the magnet, which is electrically conductive, acted as a floating electrode in each case, causing an electrostatic attraction that corrupted the force measurements
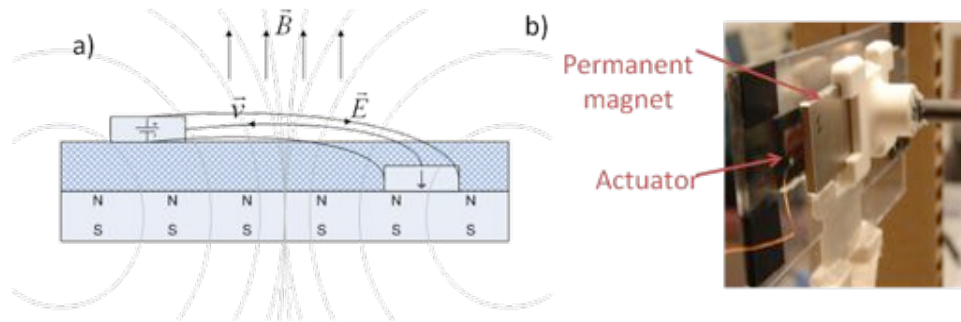


**Figure 14. (a) Schematic of DBD actuator with embedded permanent magnets. (b) Experimental set-up showing permanent bar magnet and DBD actuator.**

Alternatively, we used a Helmholtz coil pair to create a uniform magnetic field of 3.7 mT (37 Gauss) acting on the plasma actuator. While the field generated by the coils is smaller than that of the permanent magnet it is much more uniform and easily variable by controlling the current. More importantly, since the coils were far from the DBD actuator, the coils did not result in any deleterious electrostatic forces. The magnetic fields were applied in all 3 orthogonal directions (figure 15, note that $\overline{B} = \mu\overline{H}$). The results of these tests are outlined in table 1. The baseline test was performed without the presence of the applied magnetic field before and after each test. With the exception of the highlighted values, no increase (or decrease) in force was observed due to the applied magnetic field. The increased, highlighted values are a result of the induced magnetic field from the Helmholtz coil interfering with the scale's electrodynamic sensing methods. When the actuator was removed, a ~5 mg change in the force still occurred when the magnetic field was applied; it was not due to the magnetic field interaction with the actuator, but instead with the balance electronics.

Although showing little effect under the current experimental conditions (room temperature, 1 atmosphere) it is believed that the addition of a magnetic field may be beneficial at lower pressure. In our current experimental setup the ion mobility is low and as a result the particle's velocities are small. However, at lower pressures the magnetic force component can be comparable to that of the electric component (e.g. Hall thrusters) due to an increase in ion mobility. Likewise, as ion mobility is increased the number of neutral particles that become ionized may also be increased through electron trapping.
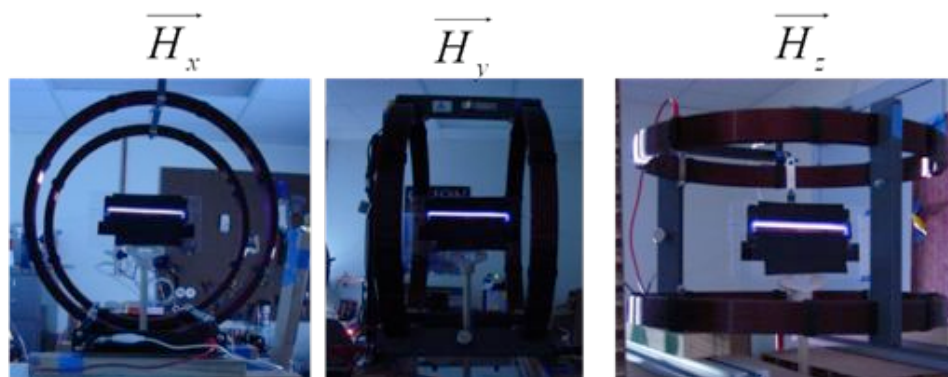
**Figure 15. Experimental set-up of Helmholtz coil tests showing the applied magnetic field oriented in the x-, y- and z-directions. The induced field is aligned along the axis through the center of two coils.**

**Table 1. Force readings with and without the externally applied magnetic field.**

|                    | $H_x$   | $H_y$   | $H_z$   |
|--------------------|---------|---------|---------|
| Baseline           | 65.9 mg | 62.1 mg | 63.2 mg |
| B-field (Test 1)   | 65.2 mg | 64.1 mg | 68.9 mg |
| B-field (Test 2)   | 65.5 mg | 62.4 mg | 68.9 mg |
| Post-test Baseline | 65.3 mg | 62.7 mg | 64.1 mg |

## B. Material Selection

### 1. *Dielectric Materials*

A large number of insulating materials exist for consideration for the dielectric barrier layer; however there are desirable properties that are of primary focus. Material properties of primary interest include high dielectric strength, high thermal conductivity, and low [relative] permittivity. The importance of the barrier layer cannot be over emphasized; the cause of device failure is almost always due to dielectric breakdown. Large electric fields promote erosion, and several ion species are constantly bombarding the dielectric barrier surface. The barrier should be resistant to chemical degradation as well. The diversity of potential materials available provides a large spread of barrier layer properties to investigate.

A broad list of potential insulation materials for use as the dielectric barrier is provided in table 2. Plastics, rubbers, and hybrid (elastomers, polymers) materials have been tested. An ideal barrier should be able to sustain plasma discharge and have low density. Thin materials are investigated to minimize the actuator mass, and it was found that dielectric strength does not scale linearly with material thickness. In order for the material to be a 'successful' dielectric barrier, it must be able to sustain plasma at voltages exceeding ~13 kVpp. Materials that could do so are indicated as 'successful' in the table. Materials that could not sustain plasma at voltages over ~13 kVpp were considered unsuccessful for use in the application at hand.

Acrylic is popularly used for the dielectric, though can only sustain plasma at high voltages using thick layers (> 1 mm). Kapton is a popular polyimide that can sustain plasma with sub-millimeter thicknesses, but only at relatively lower voltages. PDMS, a silicone-based elastomer, also provided a usable dielectric barrier at high voltages using about 1 mm thick sample. Cirlex and Torlon are two plastics that sustain plasma discharge but also require thick samples. The most promising candidate material for the dielectric barrier is 250 μm-thick (10 mil) high-purity silicone-rubber. This material was able to sustain discharge at voltages up to 16 kVpp; no other materials could reach these voltages unless they are significantly thicker. Silicone rubber was used for the majority of the WEAV experiments and demonstrations.

**Table 2. Insulation materials investigated for use as the dielectric barrier layer**

| Material | Thickness (μm) | Success |
|---|---|---|
| Acetal Copolymer Film | ~ 120 | No |
| Acrylic | 500, 1000, 3000 | Yes |
| Balloon (latex rubber) | < 100 | No |
| BOPP [Biaxially oriented poly-propylene] | 50 | No |
| Cirlex | 254, 2540 | Yes, Yes |
| Copper roll backing | ~ 50 | No |
| Craft/scrapbook Paper (3 types) | ~ 50 | No |
| FR-4 | 127 | No |
| Freezer Paper | < 100 | No |
| High melting- temp. wax | ~ 100 | No |
| Kapton© | 127 | No |
| Kapton© (silicone coated) | 114 | No |
| Kapton© (thermally conductive) | 50.8 | No |
| PDMS (Polydimethylsiloxane) | ~ 1000 | Yes |
| PEEK | 127, 250 | No |
| PET | 127 | No |
| Polyester film (one sided silicone) | 69 | No |
| Silicone (one sided) paper | 63 | No |
| Silicone rubber (high-purity) | 127, 254 | Yes, No |
| Teflon (PTFE) | 127, 254 | No |
| Teflon (with silicone adhesive) | 90, 292 | No |
| Torlon | 250 | Yes |
| Ultra high-temp. flexible Mica | 102 | No |
| Wax Paper | < 100 | No |

2. *Flexible Materials*

Silicone rubber, PDMS and Kapton were also of interest for their flexibility. Flexible substrates/dielectrics were investigated with hope that the actuators could be implemented on curved structures and surfaces. PDMS was tested in order to embed one or more of the electrodes within. The goal was to create the WEAV body out of the dielectric layer to minimize the amount of material (i.e., minimize weight) required to manufacture the vehicle. A light-weight skeleton would create a supporting structure around which the PDMS-embedded actuators could be attached. Figure 16a demonstrates the shape conforming ability of these materials, while figure 16b highlights the successful embedding of electrodes into cured PDMS.
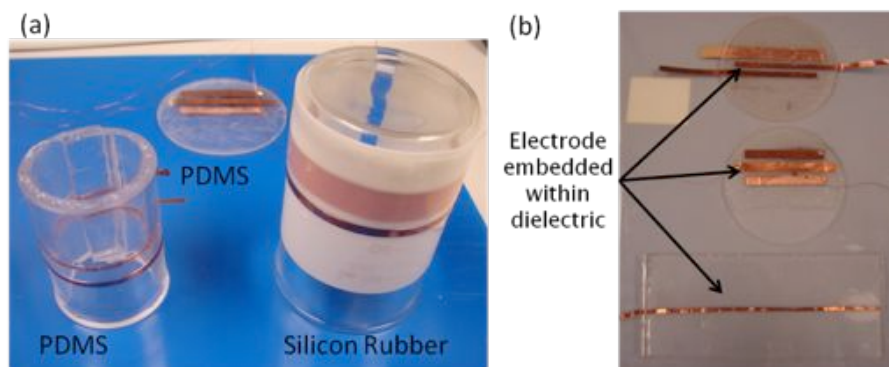
**Figure 16.  (a) Dielectric materials demonstrating flexibility around curved surfaces. (b) Embedded electrodes cured into PDMS.**

3.  *Dielectric Thickness*

   With the promising results shown using silicone rubber, the impact of the dielectric's thickness on the actuator's performance was explored. Samples have thicknesses of 10, 20, 40, and 60 mils and each have a nominal density of 1.03 g m$^{-3}$. It was observed that higher voltages and corresponding higher forces were achievable by increasing the dielectric thickness. The thrust or force was found to follow a power law for low voltages, though eventually saturates with further increase in voltage and consequently power (figure 17). The thickness of the material was observed to have a drastic impact on the saturation voltage and resulting forces. These results would indicate naively, that a thicker dielectric would be the obvious choice in the WEAV design since a high thrust output with minimal power consumption was desired. However, the increased force associated with the use of thicker dielectrics is significantly offset be the increased weight of the actuator as shown in figure 18, which provides a plot of the thrust per dielectric weight.  On a thrust to weight basis, calculated using equation 3, thinner dielectrics are clearly more favorable. In equation 3, $\forall$  represents the volume of the dielectric while $\rho$ is the material density.

$$Thrust\!\!\left/\!\!Weight\right. = \frac{f}{\forall_{dielectric} \times \rho_{dielectric}}$$
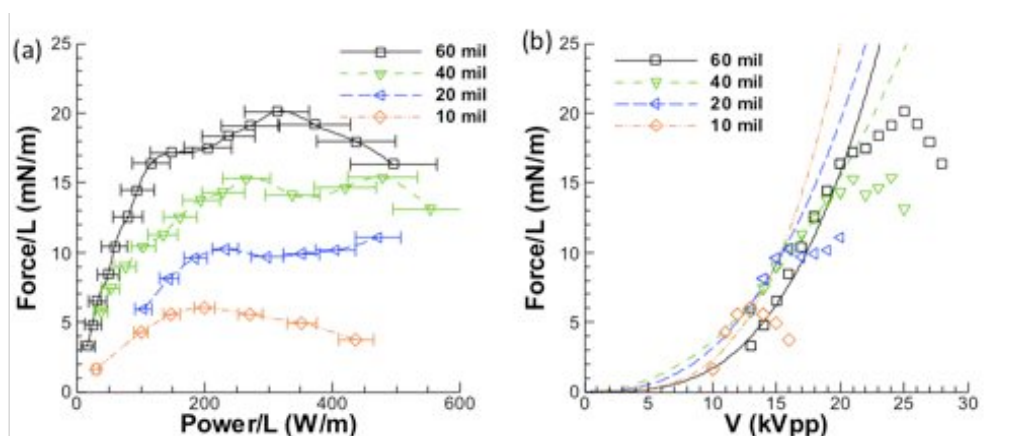
(3)



**Figure 17.  Force as a function of (a) power and (b) voltage for actuators using various thicknesses of silicon rubber for the dielectric**
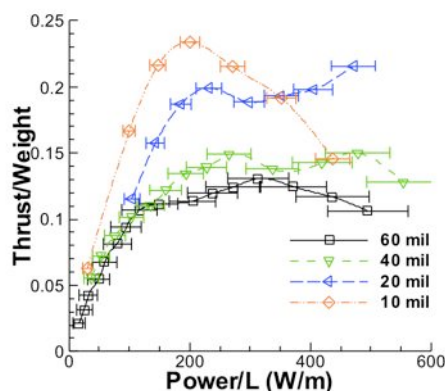
**Figure 18. Thrust to actuator weight ratio as a function of voltage for varying thickness of silicon rubber actuators.**

### 4. - *Ferroelectric*

Up to this point, dielectrics with modest values (3~10) of relative dielectric constants have been investigated. To test the effects of extremely high dielectric constants, the use of a ferroelectric (modified Lead Zirconate-Titanate, PZT) material as a dielectric was investigated. The ferroelectric sample has a nominal relative dielectric constant of 1750.

It was found that the ferroelectric material allowed for a discharge ignition at a much lower input voltage as compared to materials of the similar thickness with lower dielectric constants. Lower voltages would certainly simplify the design of an onboard power supply. A representative picture of the discharge generated is shown in figure 19a for an input voltage of 3.5 kVpp at 5 kHz. As shown in the figure the discharge is concentrated around the exposed electrode's edge. At higher voltages, for this thickness of ferroelectric, dielectric heating became an issue with temperatures reaching ~200 $^{\circ}$C after only 10's of seconds of operation. At this point, keeping the adhesively backed copper electrode adhered to the surface was challenging. Since the thrust produced is directly tied to the applied voltage, no measurable force was detected over the range of inputs tested (1.5 to 3.5 kVpp at 14 kHz).
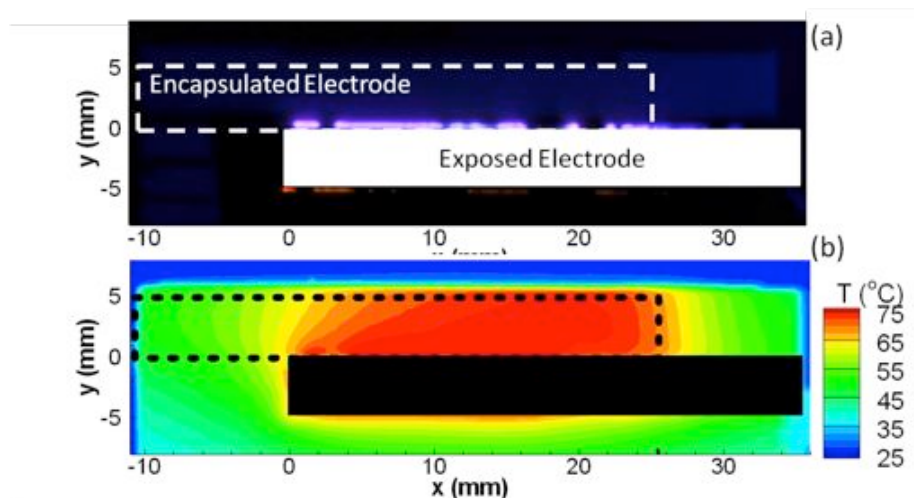


**Figure 19. Picture of plasma discharge (a) and corresponding surface temperature (b) for a 3.5 kVpp, 5kHz sinusoidal input. Temperature measurement is taken after 300 seconds of operation.**

With no force being measured, the dielectric heating of the device was investigated. An infrared camera was used to make surface temperature measurements over a range of voltages (1.5 to 4 kVpp) at 5 kHz, as well as over a range of frequencies (DC to 14 kHz) at 3 kVpp. Figure 19b shows a representative surface temperature distribution

after 300 seconds of operation.  Looking at a time trace (figure 20a) for a point taken at x = 12.5 mm and y = 1.5 mm (plasma discharge region), we see that the surface temperature has a sharp initial increase and then gradually rises in temperature. The measurements shown in figure 3a correspond to an initial 5 seconds of non-actuation after which the device was turned on for 300 seconds.  Once turned off, another 40 seconds of data acquisition continued. Noting the seemingly strong dependence on frequency, a plot of the temperature rise after 300 seconds (at x = 12.5 mm, y = 1.5 mm) as a function of power shows a linear relationship proportional to 0.87 $^{\circ}$C W$^{-1}$m (figure 20b).  This proportionality is independent of the input frequency and voltage, a trend also observed by Joussot et al.[10] However, as shown in figure 20a, for a constant voltage, one may reach the same surface temperature faster using a higher frequency. The results indicate a possibility of operating at an even higher frequency to generate thermal loading at a faster timescale. This same argument also can be made for a constant frequency with a modulated voltage.
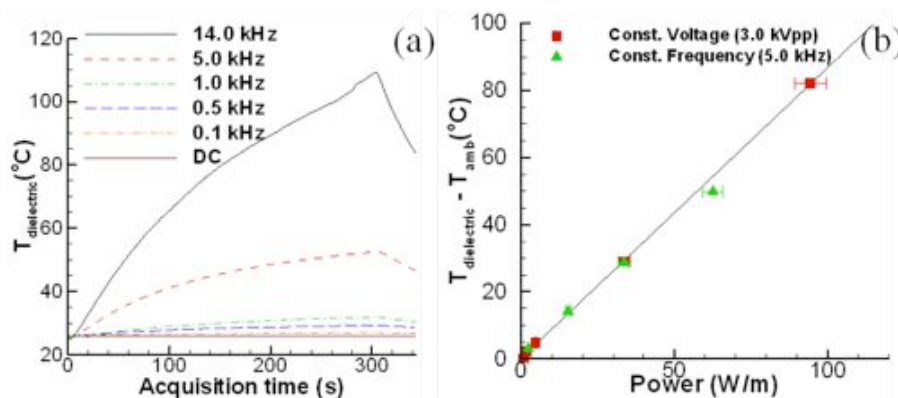


**Figure 20.  (a) Surface temperature as a function time about point 12.5 mm, 1.5 mm (x,y) for varying frequencies and (b) temperature rise in the dielectric after 300 seconds of actuation for a modulated frequency at 3 kVpp (red square) and a modulated voltage at 5kHz (green diamond).**

5. *Silica Aerogel*

   Realizing the need for an extremely light weight dielectric material, the use of silica aerogel was investigated as a candidate barrier for the WEAV design. Silica aerogel also provides the advantage of having a very low relative dielectric constant, which other researchers[11] have shown to have influence on the saturation thrust of the actuator. In general, silica aerogels consist of a complex microstructure of silicon dioxide in which air occupies a majority of it volume. For the samples tested, ~95% of the dielectric's volume was air resulting in a density ranging from 0.04 to 0.12 g cm$^{-3}$ with results being reported for samples having a density of 0.11 g cm$^{-3}$. Silica aerogels within this range of densities have a relative dielectric constant of 1.1-1.2.[12] The sample of aerogel used in this work is shown in figure 21a along with a macroscopic image of the material surface.  Small imperfections on the surface of the material are observed and vary between samples. This is considered to be a manufacturing issue and may be remedied with improved production techniques.  As an initial proof-of-concept demonstration, plasma discharge is ignited on a smaller sample of silica aerogel (figure 21b).

   The induced force produced by actuators using Kapton ($\varepsilon$ = 3.5), acrylic ($\varepsilon$ = 3), and aerogel dielectrics for various thicknesses are presented in figure 22. The open symbols indicate a direct thrust measurement made using the force balance. The closed symbols represent force measurements inferred from a control volume analysis on the induced velocity field recorded using two-component PIV. A representative time-averaged flow field is shown in figure 21c for a 36 kVpp input, where the dashed lines correspond to the sides of the control volume. The control volume analysis used is similar to that of Hoskinson et al.[9] though all three sides of the volume are considered here for completeness. The reaction force imparted to the dielectric was calculated using the conserved form of the momentum equation in the x-direction assuming the following simplifications: time independence, constant pressure, and constant density (taken as 1.184 kg m$^{-3}$). A comparison between inferred and direct thrust measurements is shown in figure 22, showing good agreement for a 3 mm thick acrylic actuator.

   The benefits of using a low dielectric constant material on thrust saturation is demonstrated in figure 22a in comparing the *t* = 6 mm thick acrylic and aerogel samples. Interestingly for this frequency, the induced force for an acrylic actuator asymptote at about 34 mN m$^{-1}$ while the silica aerogel demonstrates a much higher thrust. It should

be noted that the voltage range in this report was limited to 36 kVpp though higher voltages could have been possible using larger amplifiers. It is also notable that for a given voltage the acrylic actuator generates more thrust up to its saturation point.
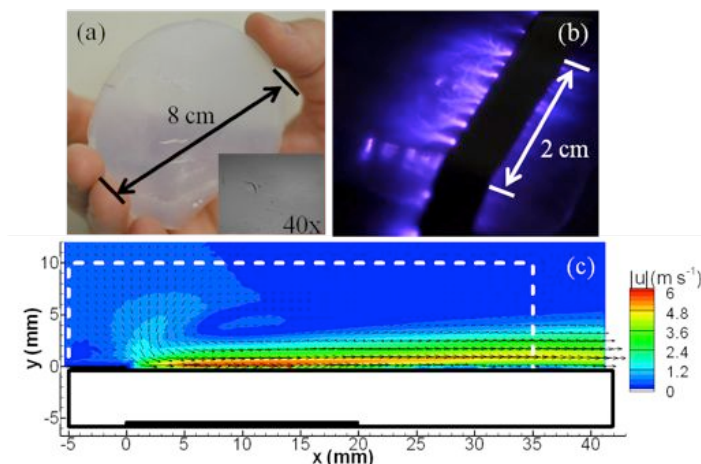


**Figure 21. A larger sample of aerogel used in reported data with 40x magnification surface topography, (b) plasma discharge on a smaller sample of silica aerogel and (c) velocity distribution measured using PIV over the aerogel sample (dashed lines indicate the boundaries of the control volume considered).[8]**

A primary benefit of the aerogel is its low density, and thus light weight. It was previously shown that higher voltages may be applied to thicker dielectrics resulting in higher force production for silicon rubber based actuators. The detrimental effect of decreasing the actuators thrust-to-weight ratio was also demonstrated. Figure 22 reiterates these trends for actuators constructed out of acrylic. The silica aerogel, however, significantly outperforms the other actuators with a force to weight basis defined by equation 3. Note that the volume of dielectric used for the values shown in figure 22b is not the same as that used in the data presented in figure 18. The density of acrylic, aerogel and Kapton were taken as 1.20 g cm$^{-3}$, 0.11 g cm$^{-3}$, and 1.42 g cm$^{-3}$, respectively. Referring to figure 22b, for a material thickness of 6 mm, the net force-to-weight ratio measured has increased from $1.8 \times 10^{-2}$ (at 30 kVpp) to $2.9 \times 10^{-1}$ (at 36 kVpp) for the acrylic and aerogel samples.[8] The net force-to-weight ratio for Kapton is $1.4 \times 10^{-1}$ at 12 kVpp. This increased thrust-to-weight basis comes with no added power consumption for the actuator as shown in figure 23.
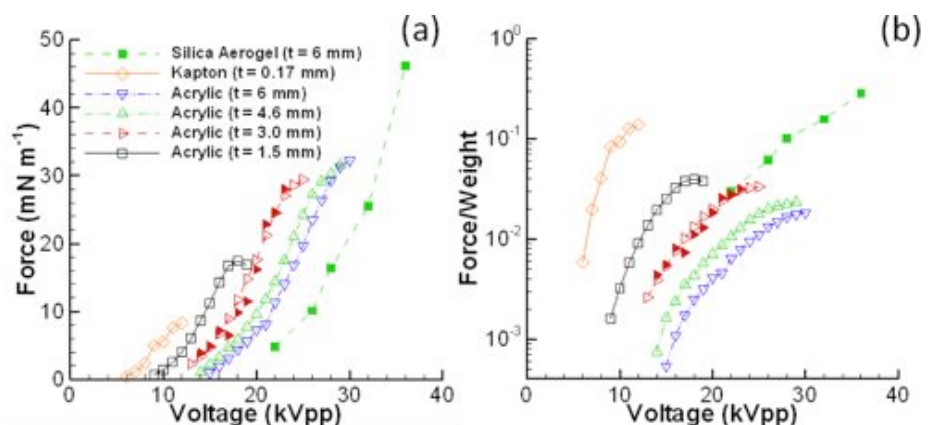


**Figure 22. Effect of the dielectric thickness as a function of voltage (a) on thrust production and (b) the ratio of force generated to the actuator weight for various dielectrics. Actuators are constructed out of for Kapton, acrylic, and silica aerogel (open symbols correspond to direct thrust measurements, while closed symbols are inferred from a control volume analysis on the induced flow field).**
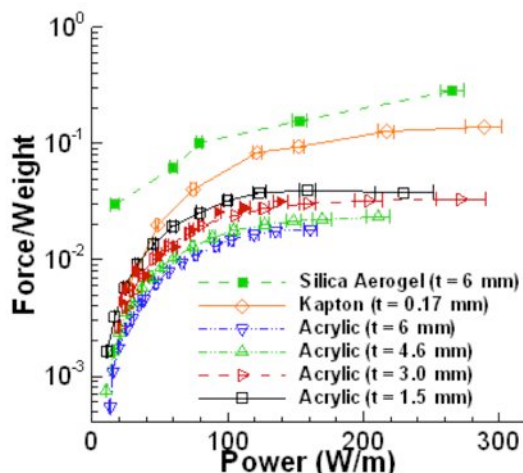
**Figure 23. The ratio of force generated to the actuator weight for various dielectrics as a function power consumption per unit length**

A recent experiment on a 10 cm long actuator plotted in figure 24 showed that **>12 g/m (0.11 N/m)** force is achievable for 3mm thick borosilicate glass. **For such thrust with aerogel a T/W>1 is possible.** While similar result is also expected for aerogel, the friability of the current samples of silica aerogel made it unsuitable for direct introduction to the WEAV design. However, the proof of concept and potential benefit of such lightweight materials as dielectrics is encouraging. As such, other more robust types of aerogels should be tested as a part of an extension of our current effort.
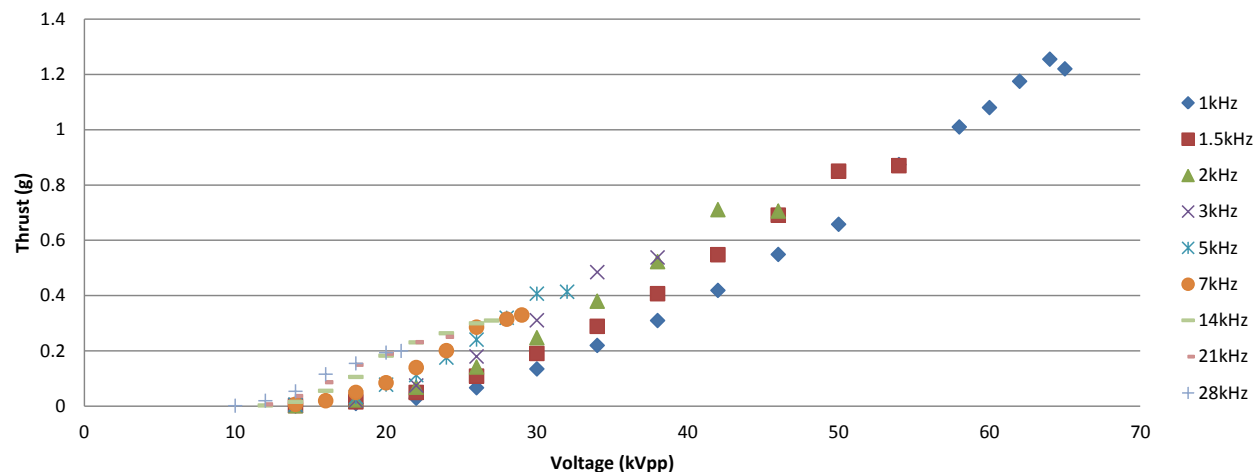


**Figure 24. Thrust measurement for 3mm borosilicate glass show >0.1 N/m thrust.**

## C. WEAV Testing
### 1. *Proof of Concept: Consistent Thrust Generation*
The first step in validation of the WEAV design was to qualitatively demonstrate that the standard plasma actuator was capable of providing sufficient force to overcome gravitational effects provided enough leverage. To demonstrate this, a plasma propelled "pinwheel" was designed and built (figure 24a). The device consisted of two plasma actuators orientated such that opposing forces were generated (figure 24b). Each actuator was cantilevered 22 cm about a rotational/pivoting center. Upon operation of the actuators the combined reaction forces produced successfully rotated the device about the pivot demonstrating the ability of the actuators to overcome gravity.
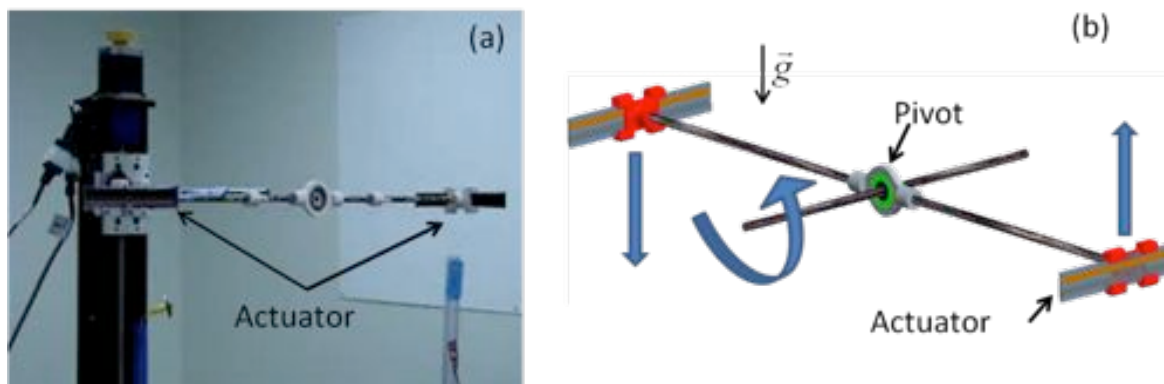
**Figure 25.**

2. *Demonstration of Pressure Differential*

The WEAV vision has top and bottom electrodes arranged radially (similar to figure 26a) to cover the circular form of the design. It was believed that by powering the top and the bottom sets of actuators separately at different potentials and/or phases that a swirling of fluid could be induced. This would provide a pressure differential which could then be harnessed to provide lift to the vehicle. To prove this concept, numerical simulations were implemented in the CFD flow modeling software Fluent$^©$. The simulations revealed that a significant decrease in pressure (~5 Pa) could be obtained on the upper surface the vehicle. The numerical work also indicated that instead of arranging the electrodes in a peristaltic manner on the lower surface, an arrangement in which one had pairs of electrodes facing each other generated a larger overall pressure differential between the two surfaces. To experimentally validate these findings, electrodes were patterned on a plate of acrylic (figure 26a) to mimic the top surface of the vehicle. Pressure taps were then placed along the surface of the acrylic at various radii staring at the center of circle.  The taps were then sampled one at time while the actuators were operational using a differential pressure transducer (Furness Controls Model 332). The transducer had a full scale range of ±25 Pa. In contradiction with the numerical results, a positive pressure was measured along surface of the plate. The pressure was found to be a function of radius with the pressure increasing as the radii was increased. A more rigorous study on the pressure distribution is documented in Section VI.
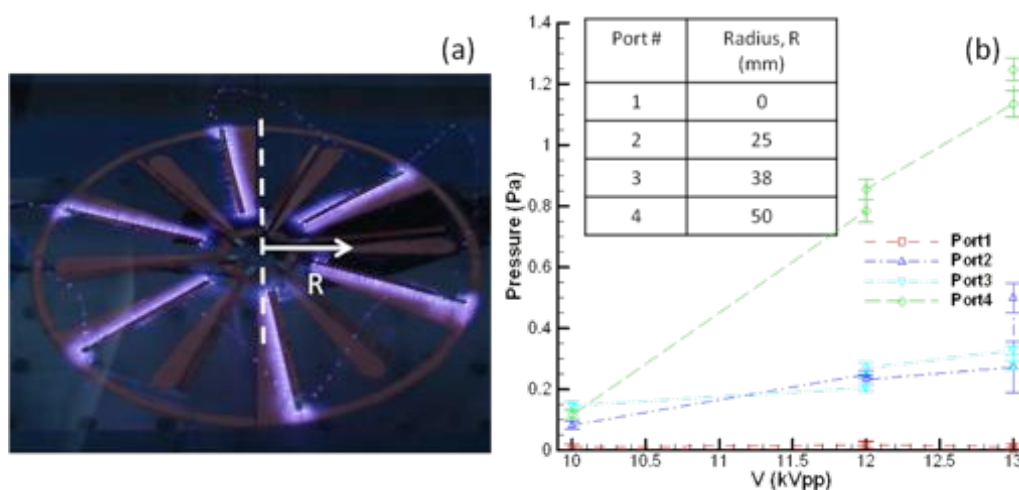


**Figure 26. (a) Circular electrode arrangement for pressure differential experiments and (b) plotted data.**

3. *Construction of preliminary WEAV Prototypes*

Simplified designs of the WEAV vision were built to evaluate its potential flight capabilities. These early prototypes consisted of a thin ring of dielectric (the actuator) with a supporting lid, which helped maintain the structural form (figure 27). The dielectric used for these prototypes was 10 mil thick silicon rubber.  As shown in previous sections, 10 mil thick silicon rubber demonstrated the highest thrust-to-weight ratio, with the exception of silica aerogel. This geometry was subject to thorough investigation both experimentally and numerically. In the end,

both methods revealed the importance of uniformity in the manufacturing of these prototypes. Since these devices were built by hand, this was a problem that continually plagued and hindered the devices from successfully lifting off the ground. This resulted in the efforts (discussed in Section V) to create a reproducible prototype using more automated methods.
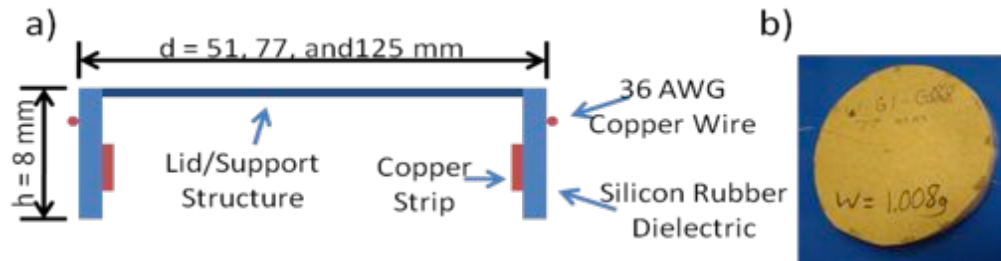


**Figure 27. a) Dimensional schematic of WEAV prototypes. b) Example of WEAV prototype.**

Even with such crude manufacturing techniques a successful liftoff was achieved using an external power supply (figure 28). **The prototype was able to hover a few millimeters above the surface for a sustained duration (~3 minutes). Prototypes of varying radius were also successfully "flown", demonstrating that WEAV is scalable.** The fact that the lift off was never more than a few millimeters from the surface, eludes that ground effects may be playing a strong role in overall thrust production. The following section outlines experiments carried out to investigate these mechanisms.
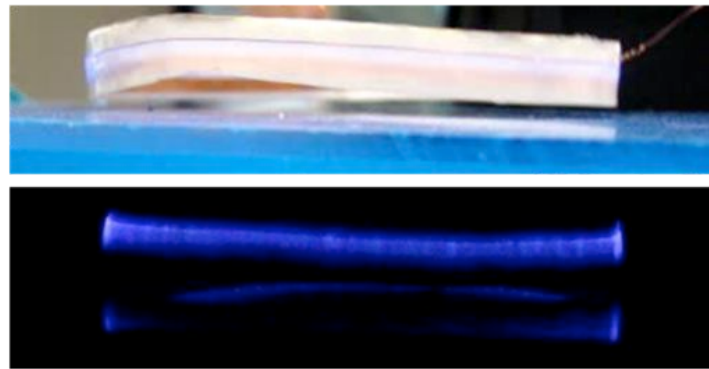


**Figure 24. Demonstration of successful liftoff of WEAV prototype**

4. *Ground Effects*

Ground effects were tested using a plate (acrylic) attached to a traverse. The distance between the device and the plate was varied and force readings were taken at each height location. In order to record force measurements, this test was conducted in an inverted configuration (figure 30a). The WEAV was mounted 'upside down' on the balance such that the reaction force (i.e., thrust) was directed downward onto the scale for a force reading (figure 30b). The 'ground' plate was initially positioned just above the WEAV prototype. This was considered the 'zero' position, equivalent to the WEAV sitting on the ground surface. The plate was vertically incremented above the prototype, increasing the distance between the device and the simulated ground plane.

Force measurements were recorded at several discrete vertical locations, and the trust-to-weight ratio was computed and plotted versus the distance between the device and ground plate as illustrated in figure 31a. An exponential increase in the force was measured as the ground plate approached the prototype. As observed in the plot, the thrust-to-weight ratio exceeds unity (required for liftoff) only when the ground plate is within a millimeter or two of the WEAV. The devices that successfully lifted off the ground hovered about 1-2 mm above the ground surface. This value agrees well with the data in the plot, indicating that the ground is indeed assisting in the force.
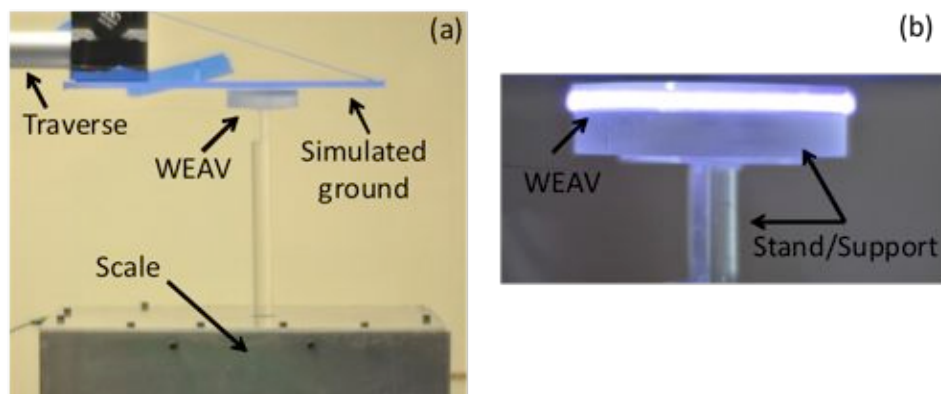
**Figure 25. (a) Experimental set-up to simulate ground effects on the measured thrust. (b) Close-up view of prototype inverted and mounted to measure the reaction thrust using a digital balance.**

The power consumed by the device was also recorded at each test position. The power data is plotted in figure 30b against the distance between the device and ground plane. The power remains approximately constant for each voltage tested, independent of the distance to the ground plate. For a constant voltage, a constant power should provide constant thrust. The force increase must be due to recirculation effects when the device is near the ground surface. Once the ground surface is ~10 mm above the prototype, the thrust measured remains roughly constant indicating the actual thrust-to-weight ratio without ground effects.
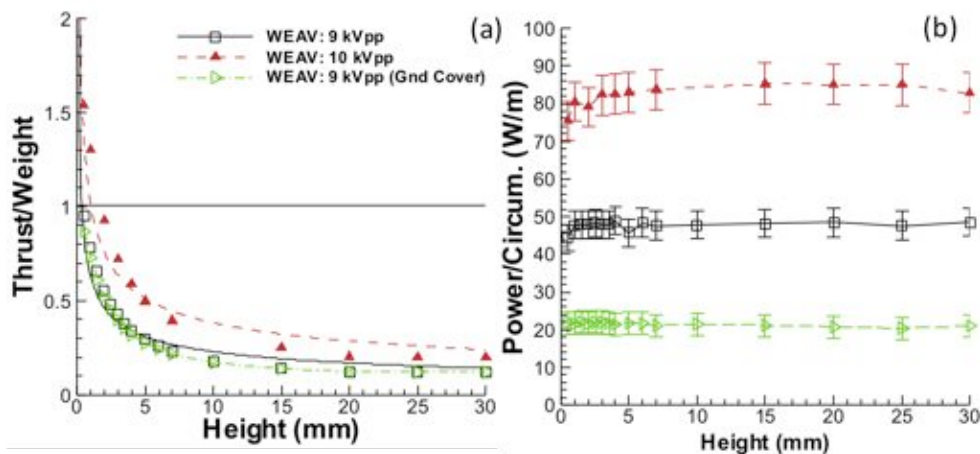


**Figure 26. (a) Thrust-to-weight ratio plotted against distance between the prototype and ground plane. (b) Power consumed at each position for each of three voltages tested, indicating nearly constant power regardless of the ground proximity.**

5. *WEAV Designs*

Figure 31 shows several cylindrical designs options for WEAV. Several of these designs were tested and the experimental data are documented in figure 32. These designs are numerically described in further details in Section III.
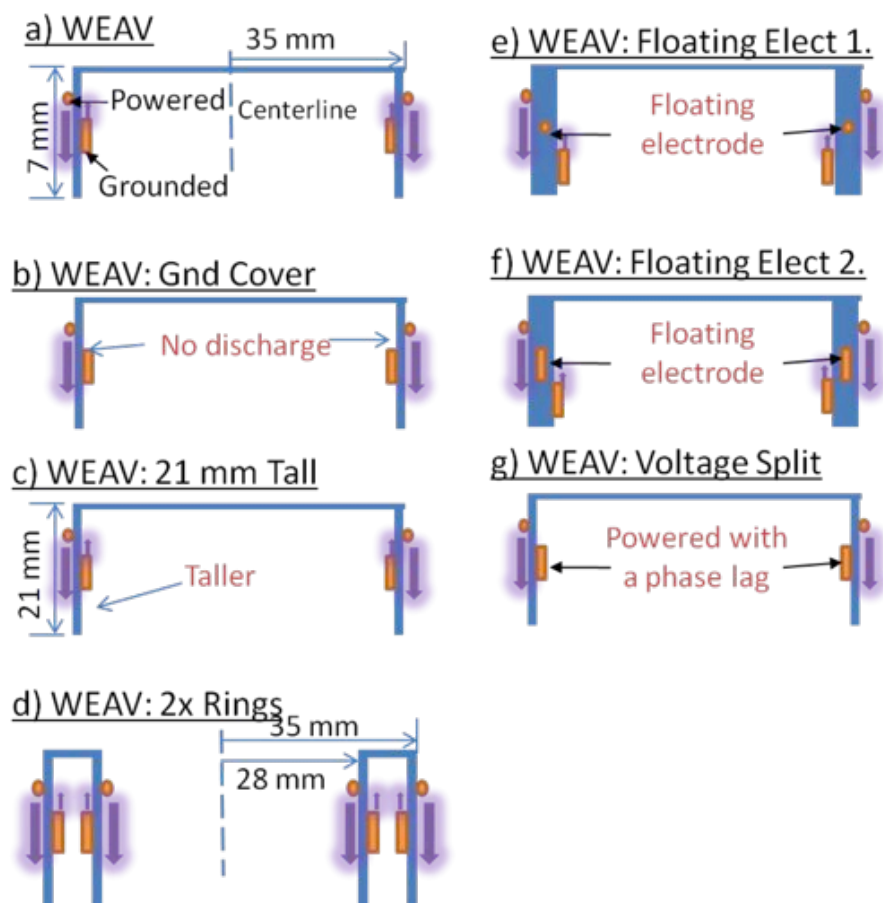
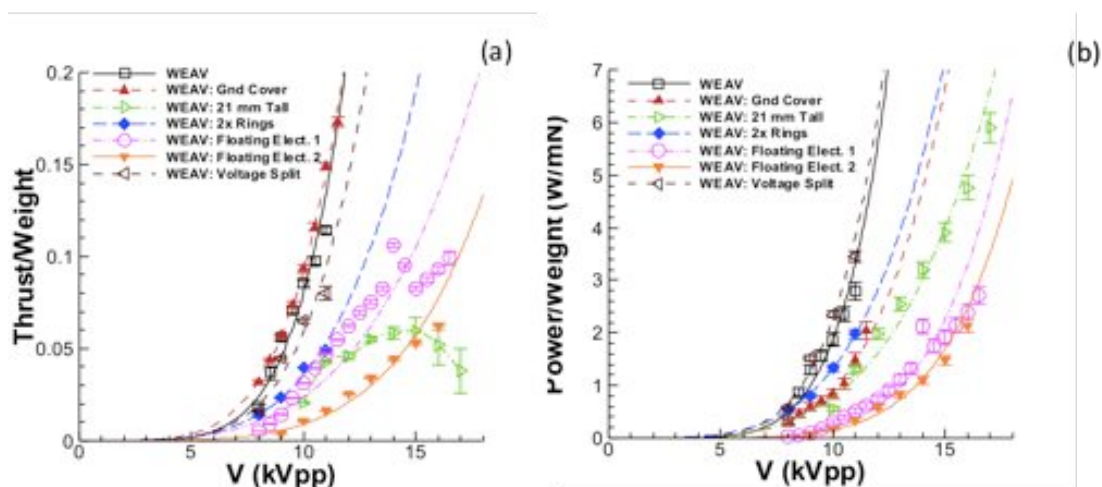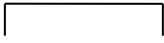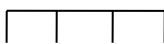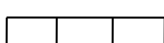**Figure 27. Various cylindrical WEAV designs.**



**Figure 28.  WEAV test data.**

## III. Simulation of various cylindrical wingless geometries for aerodynamics and flight dynamics.

### A. Geometry

Seven geometries were studied numerically. All of these designs are listed in table 3. The designs were selected to test for combinations of certain geometric features. Design 1 was the most basic design consisting of a single cylinder wall. Design 3 consisted of an inner and an outer cylinder, and Design 5 was identical except for the fact that the space between the inner and outer cylinders was closed. The even-numbered designs corresponded to the next lowest odd-numbered designs, with the modification that the top was no longer fully closed, but contained a hole. The radius of this hole corresponded to the size of the inner cylinder radius. One set of dimensions was tested for the 2-D simulations. The outer radius was taken as 70 mm and the inner radius was 35 mm. The cylinder height was taken as 10 mm.

**Table 3. WEAV designs used for numerical study.**

| Design Number | Description | Schematic (Side View) |
|---|---|---|
| 1 | Single Cylinder Closed Top | |
| 2 | Single Cylinder Open Top | |
| 3 | Double Cylinder Closed Top, Open Bottom | |
| 4 | Double Cylinder Open Top, Open Bottom | |
| 5 | Double Cylinder Closed Top, Closed Bottom | |
| 6 | Double Cylinder Open Top, Closed Bottom | |

### B. Numerical Methodology

The flow simulations were carried out using the commercial Fluent software. The computational grids compatible with Fluent were generated using the ICEM CFD software which is a part of the ANSYS package. One-way coupling between the fluid and the plasma was assumed. In this approximation, any feedback mechanisms from the fluid to the plasma are assumed to be negligible. This assumption allows the Navier-Stokes equations for the fluid flow to be solved separately from the plasma. The effect of the plasma on the flow is included in the body force term in the fluid momentum equation.

Various models exist in literature for the body force applied by the plasma on the fluid. In this study, the reduced order exponential model of Singh and Roy[13] was used. In this model, the plasma body force is given in the form

$$F_x = F_{x0}\phi_0^4 \exp\left(-\left\{[x - x_0 - (y - y_0)]/y\right\}^2 - \beta_x[y - y_0]^2\right)$$

$$F_y = F_{y0}\phi_0^4 \exp\left(-[(x - x_0)/y]^2 - \beta_y[y - y_0]^2\right) \tag{3}$$

The body force is a function of the applied voltage and distance from the actuator. The x-coordinate in equation 3 is parallel and the y-coordinate is perpendicular to the actuator surface. The parameters $F_{x0}$, $F_{y0}$, $\beta_x$ and $\beta_y$ are constants determined by curve-fitting first principles solution data from the in-house finite element MIG code. The force was applied in Fluent using the user-defined function (UDF) interface.

### C. Flow Simulation Results

1. *2-D Simulations*

The original 6 designs were investigated numerically at distances of 1 cm and 100 cm from the ground. Figure 33 shows the time-averaged pressure fields with the velocity vector fields on top, while figure 34 shows the same time-averaged data at 1 cm. From the figures, we can observe that for all the designs, the pressure on the bottom is higher in the 1 cm case, showing that the ground effect will aid the vehicle. The recirculation of the fluid reduces the pressure on the bottom, most notably for designs 2, 3 and 4, but also for the other three designs.

Design 1 shows the highest pressure on the bottom for both the 1 cm and 100 cm condition. Design 2 is overall the worst from a pressure standpoint, because the hole on the top seems to release a lot of the pressure that design 1 had. Design 3 at 100 cm has 2 vortical structures between the inner and outer cylinder region. At 1 cm, a third recirculation forms due to the ground inside the inner cylinder region. All the designs with open tops form a fountain at 1 cm that goes through the open hole. At 100 cm, the three designs with the highest pressure drop due to recirculation are designs 1, 3 and 4. This is likely due to the actuator design, where the outer side of the wall has a downward force and the inner side has an upward force. Designs 2, 5 and 6, which do not have this kind of force do not appear to have as large of a pressure drop due to the recirculation at 100 cm as the other three designs. Looking closely at the designs with the high recirculation, we can also observe that the recirculation also causes trapping of some fluid in the corners, raising the pressure in the region. This effect is the most pronounced in designs 3 and 4, where the length scale of the two counter-rotating vortices is of the order of the difference between the outer and the inner cylinders.

Based on the results from these runs, designs 1, 3 and 4 showed the most promise and were down-selected for further analysis. 2-D simulations with a 2 m/s wind gust were performed for the three remaining designs. The wind gust cases were simulated at a height of 100 cm from the ground.

Figure 35 shows the results for the wind gust simulations. In all three cases, we can observe a stagnation point on the side of the vehicle facing the wind, accompanied by a pressure rise. In the case of design 4, there is a fairly significant pressure rise under the bottom part that would create a pitch or roll moment on the vehicle depending on the flight direction. The 2-D results showed that the wind gust was strong enough the drastically alter the pressure around the vehicle.
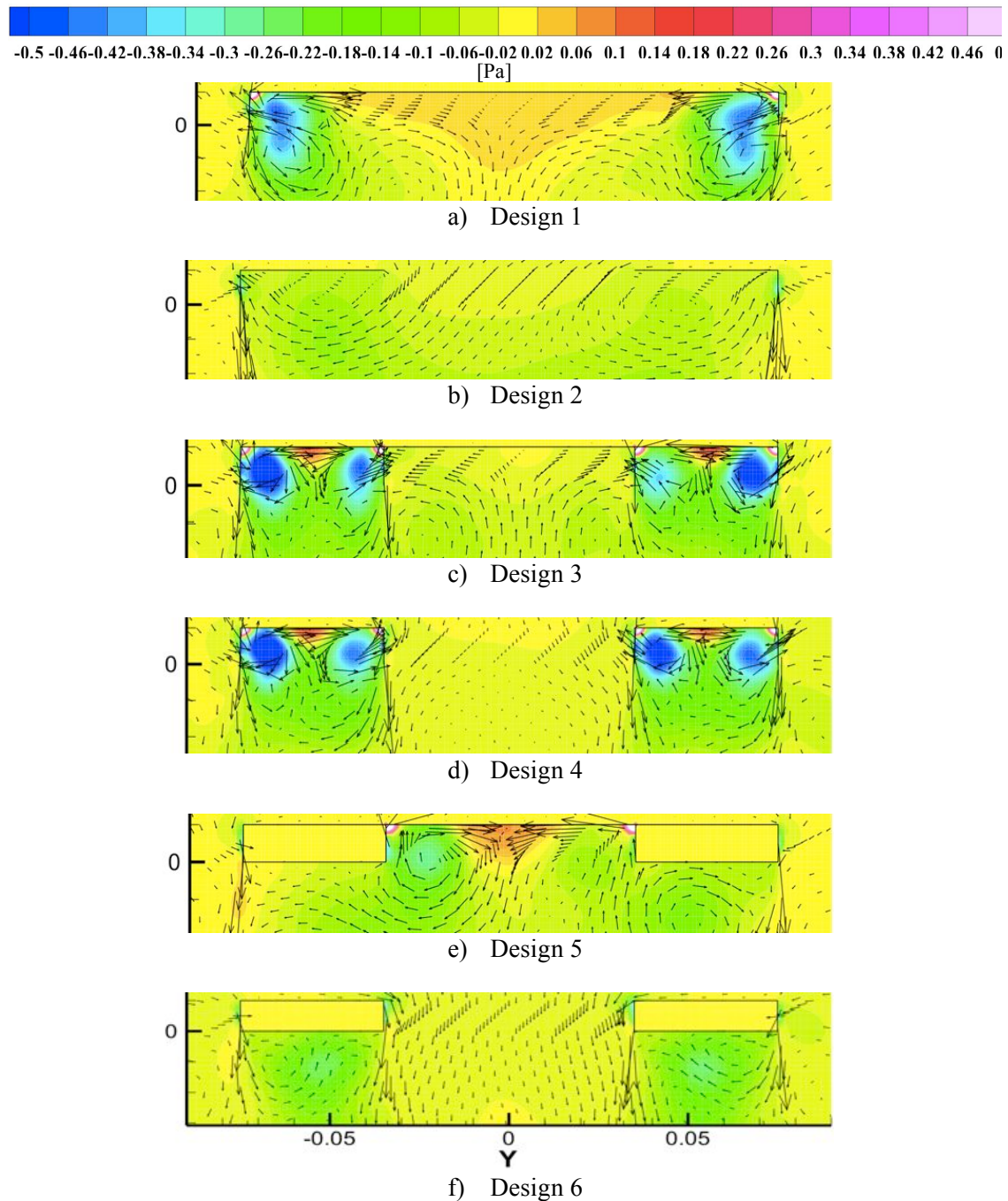
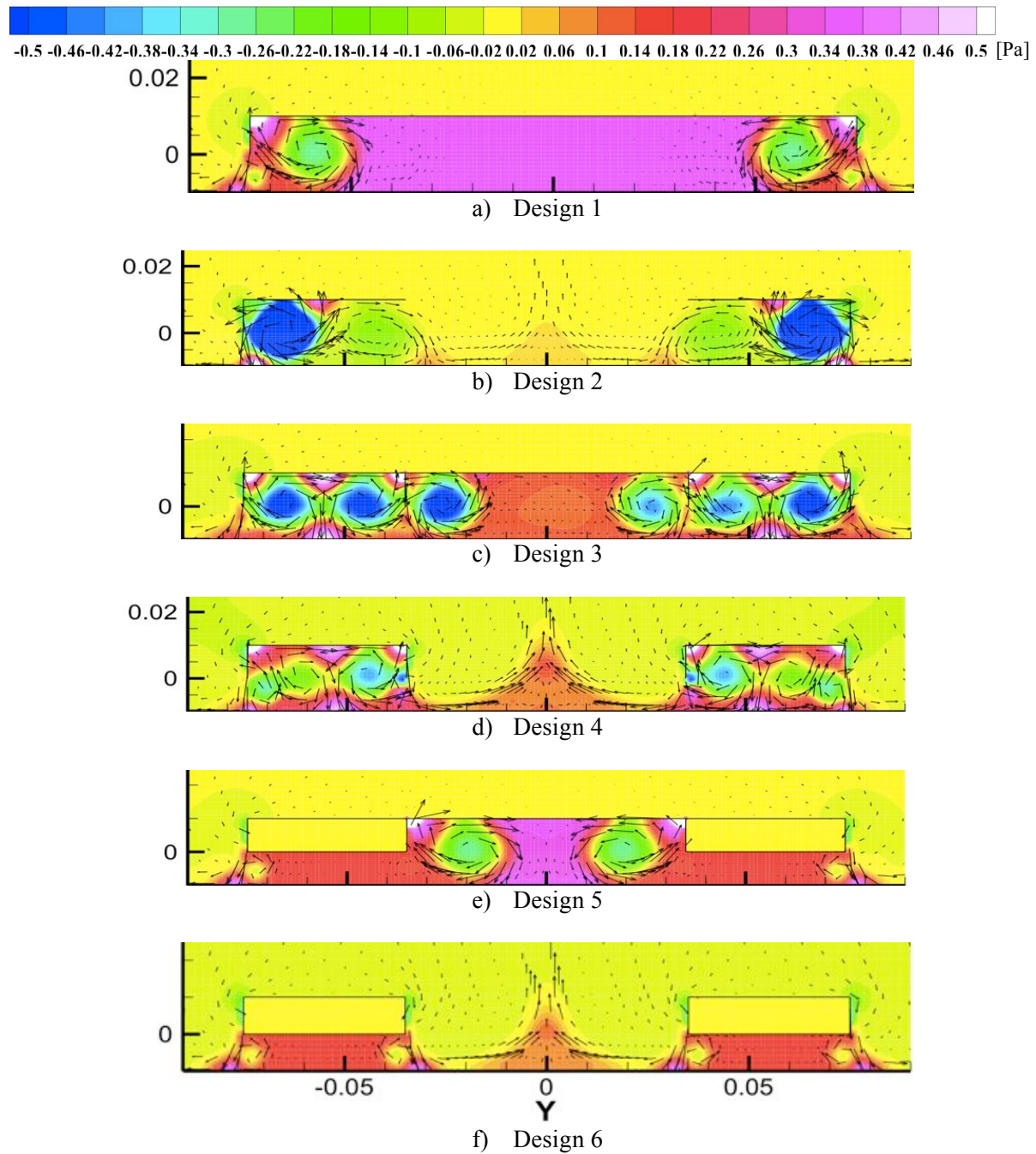**Figure 33. Time averaged pressure contours and velocity vectors for WEAV at 100 cm above ground.**

-0.5 -0.46 -0.42 -0.38 -0.34 -0.3 -0.26 -0.22 -0.18 -0.14 -0.1 -0.06 -0.02 0.02 0.06 0.1 0.14 0.18 0.22 0.26 0.3 0.34 0.38 0.42 0.46 0.5 [Pa]

a) Design 1

b) Design 2

c) Design 3

d) Design 4

e) Design 5

f) Design 6

**Figure 34. Time averaged pressure contours and velocity vectors for WEAV at 1 cm above ground.**

a) Design 1          b) Design 3
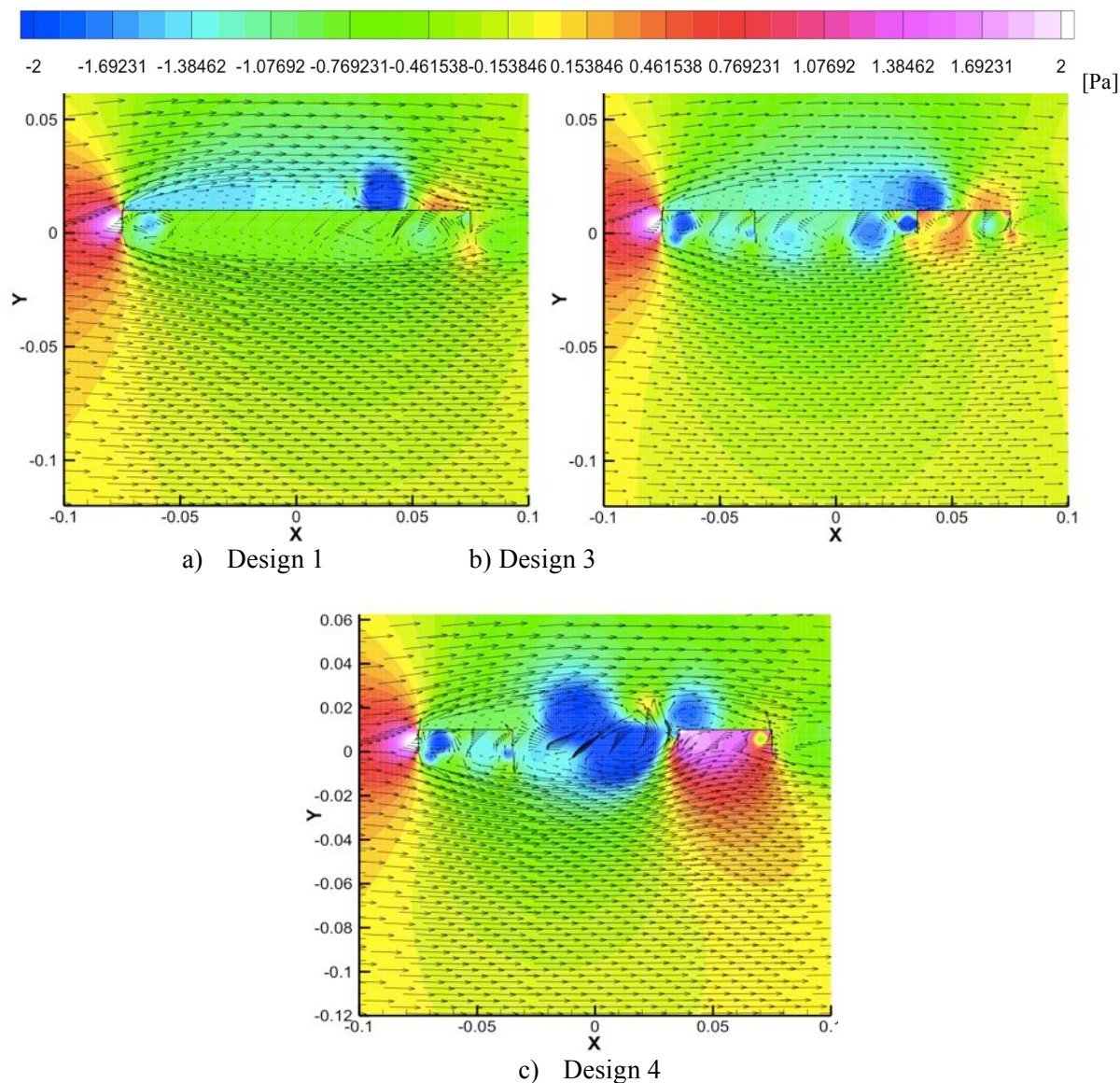


c) Design 4

**Figure 35. Pressure contours and velocity vectors for WEAV at 100 cm under 2 m/s wind gust.**

2. *3-D Simulations*

In addition to the 2-D wind gust simulations, 3-D simulations were performed for designs 1, 3 and 4 for a more physically accurate flow field. The 3-D simulations were run on four processors using parallel Fluent. Heights of 1 cm and 30 cm were considered to study the ground effect in 3-D. Height of 100 cm which was used in the 2-D case was not considered due to the grid size constraints. The 30 cm height was found to be sufficiently far from the surface to eliminate ground effects.
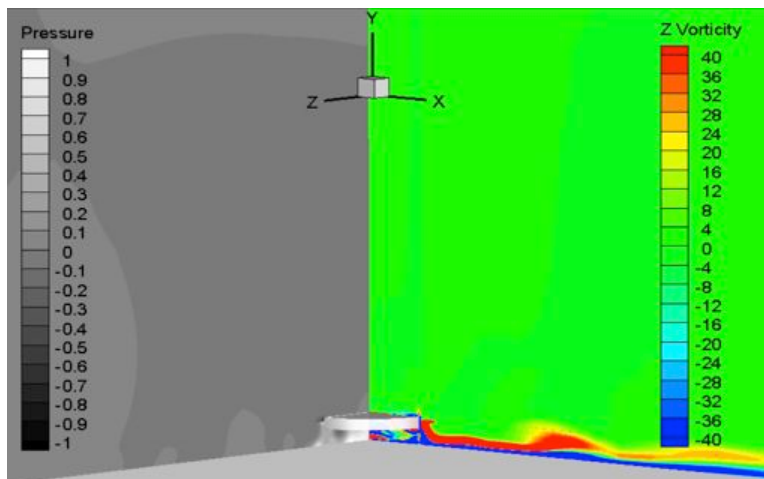
a)   Design 1 (1 cm from ground)
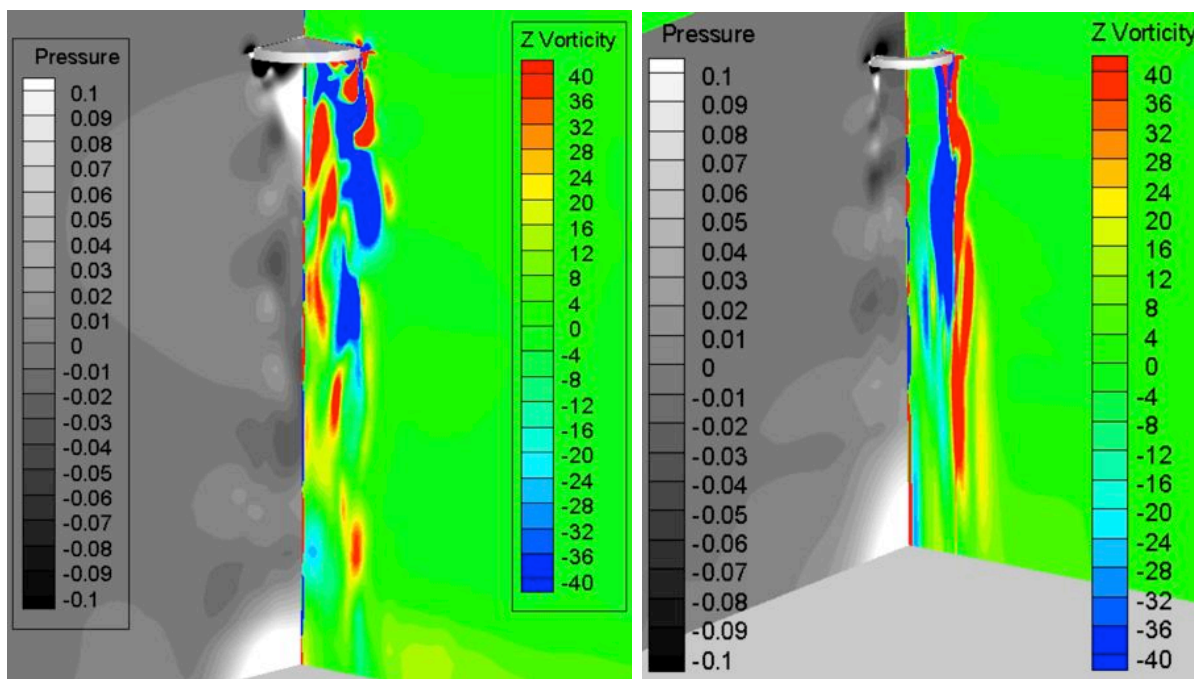


b)   Design 1 (30 cm from ground)          c) Design 4 (30 cm from ground)

**Figure 36. 3-D WEAV simulations.**

Figure 36 shows pressure and vorticity contours for three separate runs. Table 4 gives the integrated forces on the vehicle for all six runs. These results indicate that the ground enhances the net fluid force by as much as five times for design 1. For designs 3 and 4, the numerical simulations indicate that the vortices that form between the two cylinders can trap high pressure more effectively, so the loss of pressure is not as drastic. Design 4 benefits more from this effect, because the trapping is limited to the region between the two cylinders and the lid over the inner cylinder adds more weight to the vehicle.
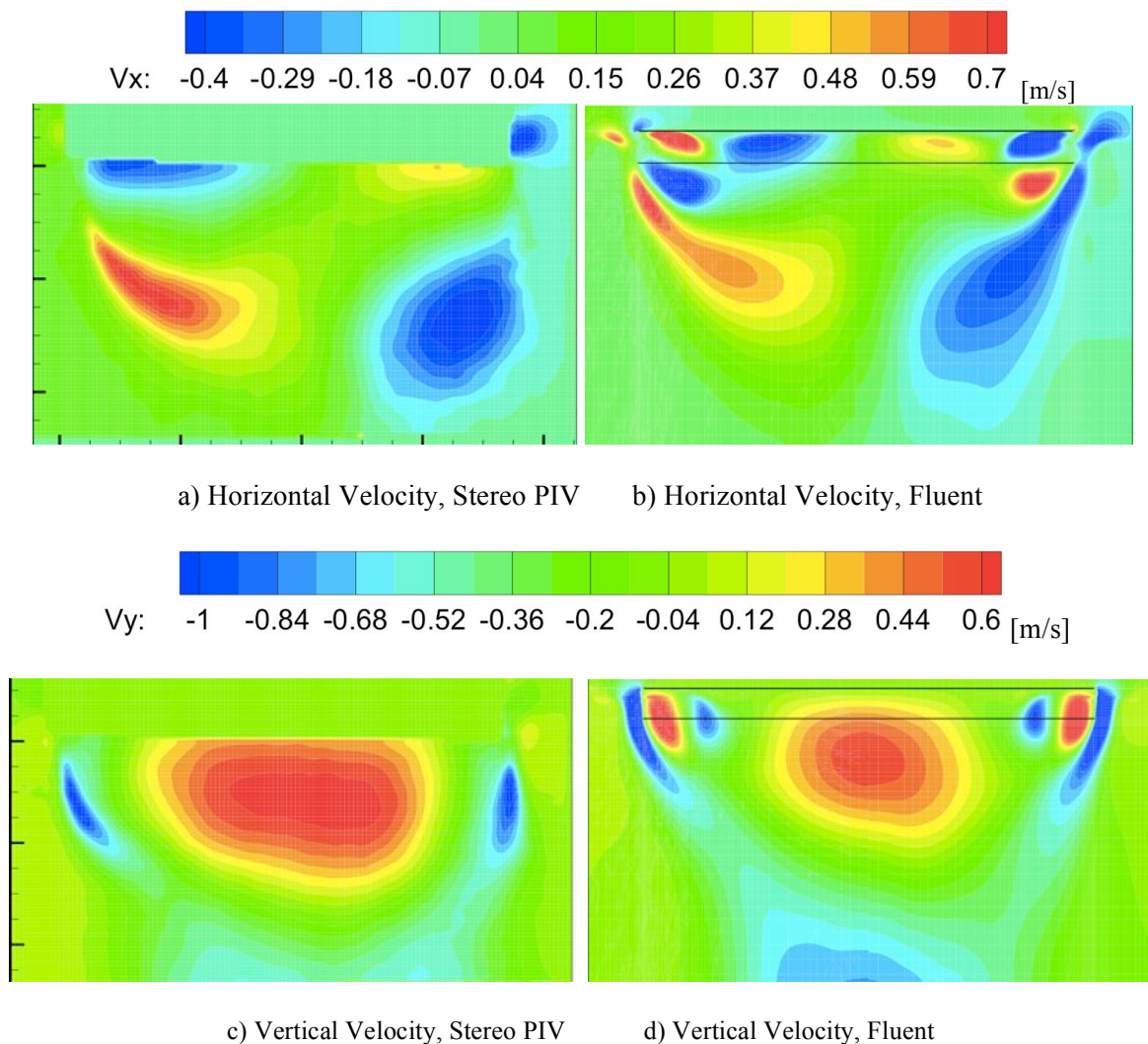
Vx:  -0.4  -0.29  -0.18  -0.07  0.04  0.15  0.26  0.37  0.48  0.59  0.7  [m/s]

a) Horizontal Velocity, Stereo PIV          b) Horizontal Velocity, Fluent

Vy:  -1  -0.84  -0.68  -0.52  -0.36  -0.2  -0.04  0.12  0.28  0.44  0.6  [m/s]

c) Vertical Velocity, Stereo PIV          d) Vertical Velocity, Fluent

**Figure 37. Comparison between 3-D simulation and PIV experiment for Design 1.**

The 3-D simulations for designs 1 and 4 without ground effect were validated against stereo PIV experiments. The comparisons are given in figures 37 and 38. The z-component of the velocity (out of plane) was negligible, which implies that the flow is axisymmetric and validates the use of 2-D simulations. From the results, it is seen that the 3-D simulations qualitatively capture the main features of the flow field. The main difference occurs for design 1 where the numerical simulation predicts the fluid to be pulled up along the inner wall, which is not observed in the PIV, and most likely means that the plasma force on the inner wall is not as strong as the force model predicts.
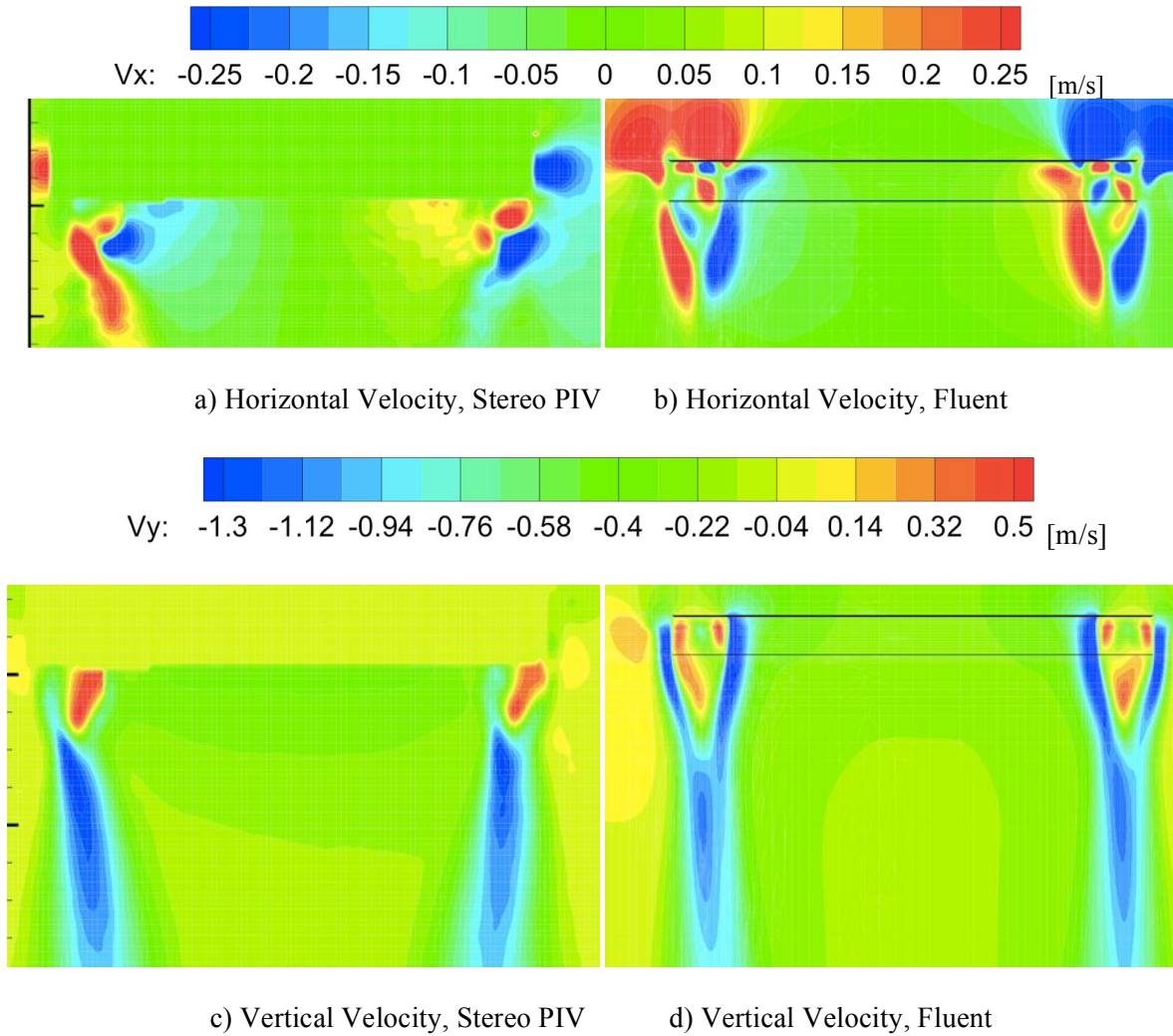
a) Horizontal Velocity, Stereo PIV          b) Horizontal Velocity, Fluent



c) Vertical Velocity, Stereo PIV          d) Vertical Velocity, Fluent

**Figure 38. Comparison between 3-D simulation and PIV experiment for Design 4.**

**Table 4. WEAV force data based on the 3-D simulations.**

| Design | 1 | | 3 | | 4 | |
|---|---|---|---|---|---|---|
| **Altitude** | 1 cm | 30 cm | 1 cm | 30 cm | 1 cm | 30 cm |
| **Net Plasma Force (mN)** | 3.3882 | 3.3882 | 4.0302 | 4.0302 | 4.0302 | 4.0302 |
| **Net Fluid Force (mN)** | 3.2322 | 0.6837 | 3.4183 | 2.6757 | 3.1752 | 2.1115 |
| **Vehicle Weight (mN)** | 6.6761 | 6.6761 | 8.8245 | 8.8245 | 6.4239 | 6.4239 |
| **Total Vehicle Force (mN)** | -0.0557 | -2.6041 | -1.3760 | -2.1187 | 0.7815 | -0.2822 |
| **T/W** | 0.9917 | 0.6099 | 0.8441 | 0.7599 | 1.1217 | 0.9561 |

**D.  Modeling of Flight Dynamics**

The 2-D simulation results for design 1 were used for modeling of flight dynamics. The flow conditions for the flight dynamics studies were the same as the 2-D simulation at a height of 100 cm. The air surrounding the vehicle was assumed to be in quiescent conditions. The vehicle had a 70 mm diameter and 10 mm height. Runs were carried

out over a time of 3 minutes, and pressure statistics on the top and bottom wall were taken at a sampling frequency of 10 Hz. The fluid component of the thrust was assumed to be directly proportional to the pressure difference between the bottom and the top walls.

### 3. *A. Time-Frequency Representation*

The net pressure on the vehicle is investigated to determine if dominant modes exist. The time-domain measurement of this net pressure is shown in figure 39. In this case, the data represents the integration of pressure across the vehicle at each instant in time. The net pressure has an average close to zero; however, it is characterized by rapid variations of large magnitude.
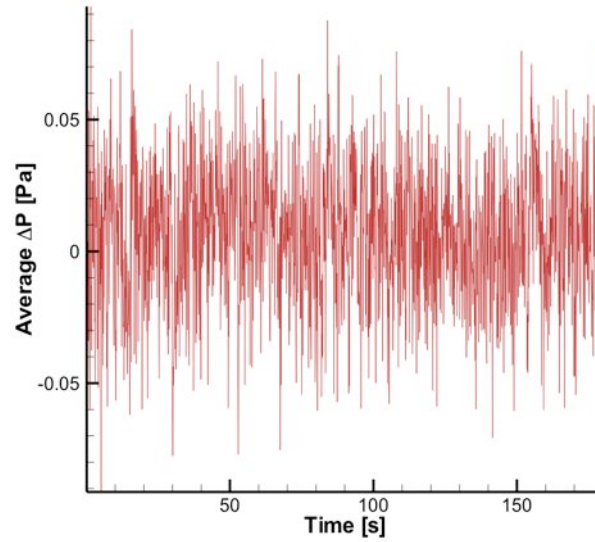


**Figure 39. Time-domain measurements of net pressure in response to constant thrust from plasma actuation.**

The frequency content of the pressure is determined using a Fourier transform as shown in figure 40. This transform demonstrates the pressure has somewhat of a high-bandwidth nature without any large peaks indicating dominant frequencies. As such, modes do not seem to be present in the pressure.
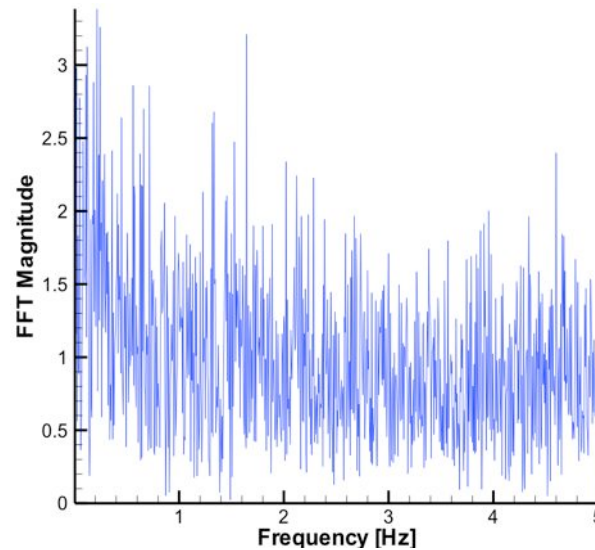


**Figure 40. Frequency-domain transform of the net pressure in response to constant thrust from plasma actuation.**

A wavelet transform is also introduced to determine any temporal nature associated with the frequency-domain content. The use of a Morlet wavelet in the transform allows the magnitude of various frequencies to be identified in the pressure at each instant in time. The resulting time-frequency-domain representation is shown in figure 41 with the scale being related to the inverse of the frequency.
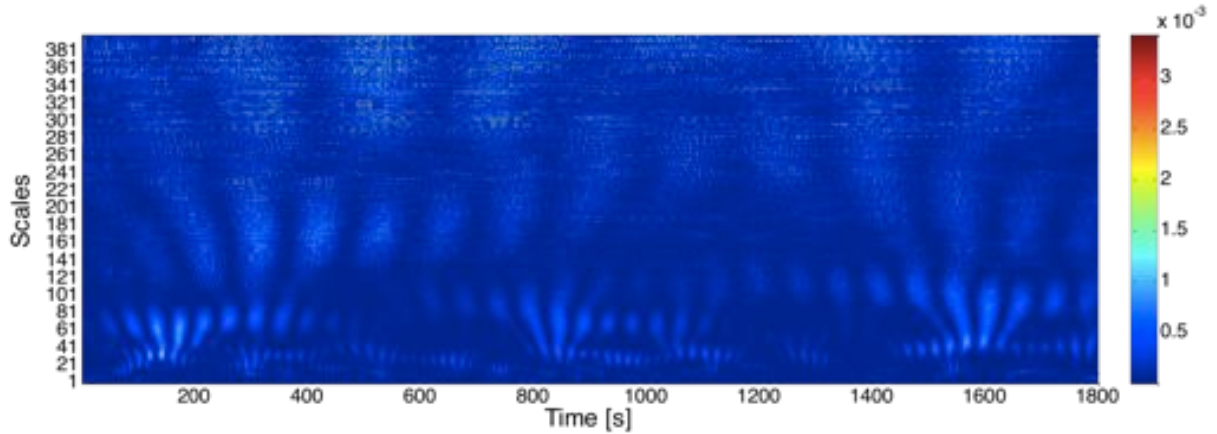


**Figure 41. Wavelet transform showing time-frequency domain of the net pressure in response to constant thrust from plasma actuation.**

The time-frequency-domain information of figure 41 presents insight into the pressure that is not immediately obvious in either the time-domain data of figure 39 or the frequency-domain data in figure 40. Specifically, the pressure has a complex periodicity involving low frequencies and high frequencies. The wavelet map shows some high-frequency content is relatively constant throughout the response with a low-frequency content appearing for a short time approximately every minute. This low-frequency content has a high magnitude and thus seems to be dominant in the flow as can somewhat be seen in figure 39 at times of 15 seconds, 85 seconds, and 155 seconds.

A low-fidelity model of the pressure can thus be generated using this periodicity coupled with a broadband response.

$$P = \begin{cases} 0.05\sin\left((2\pi/20)t\right)+0.02 \text{ broadband for } t = \left[70n : 70n+5\right] \\ 0.02 \text{ broadband elsewhere} \end{cases}$$

(2)

4. *Spatial representation*

The spatial distribution of the pressures across the vehicle is evaluated in figure 42. In particular, the net pressure at each spatial location on the vehicle is shown for three instances each 1 minute apart. The net pressure varies with time; however, the general shape of the net pressure across spatial location remains reasonably similar.
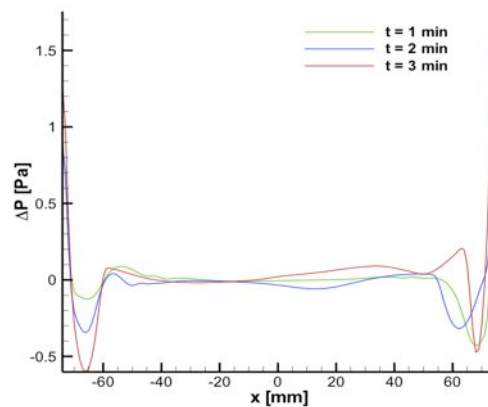


**Figure 42. Spatial variation of net pressure for 3 instances in time.**

Some localization of net pressure is indicated by the relative invariance of the pressure distribution across time. Essentially, the vehicle is affected by a high value of positive pressure near each wall and a high value of negative pressure just slightly inboard of each wall. An additional small value of positive pressure occurs over the central region of the vehicle.

A reduced-order model of the forces is generated by considering a free-body diagram shown in figure 43. This model replaces the spatially-varying force across the vehicle with 5 forces that act at distinct locations. The location of these forces is shown in figure 43 along with the area over which the pressures are integrated to get each resultant force.



**Figure 43. Free-body diagram.**

The actual representation of each has the same mathematical periodicity as the pressures. Figure 44 shows the time-domain measurements of pressure at a set of locations in each of the spatial regions from the free-body diagram.
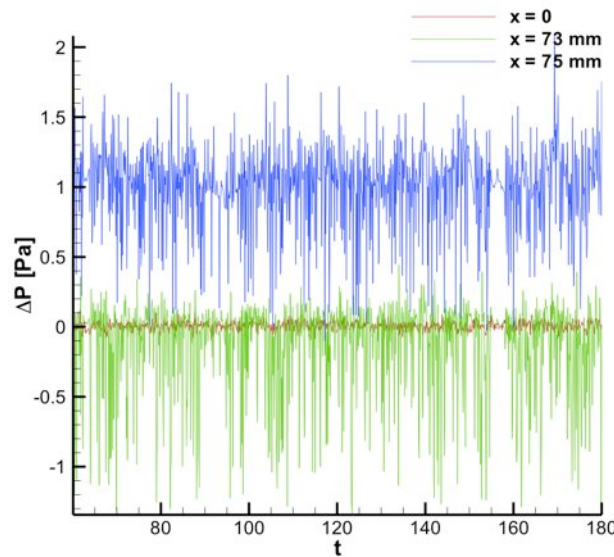


**Figure 44. Time-domain measurements of pressure at the 3 distinct regions.**

The pressure at each location has the same broadband nature with the large-magnitude low-frequency component every 70 seconds as was shown for the net pressure in figure 39. As such, the representation of the net pressure is suitable for each of the resultant pressures in figure 43. The actual magnitudes for the resultant pressures are generated from the near-wall region having an average pressure of 1 Pa with oscillations nearing 0.5 Pa, the inboard region having an average pressure of -0.5 Pa and oscillations nearing 0.5 Pa, and the central region having an average pressure of approximately 0.0 Pa with oscillations about 0.1 Pa.

   5. *Nonlinearity*

Some modeling of nonlinearity in the flight dynamics is evaluated for the transfer function from plasma actuation to pressure.[14]  In this case, the force imparted on the fluid due to plasma actuation is doubled by altering the voltage from 14 kV to 16.64 kV.  The resulting net pressures are presented in figure 45.
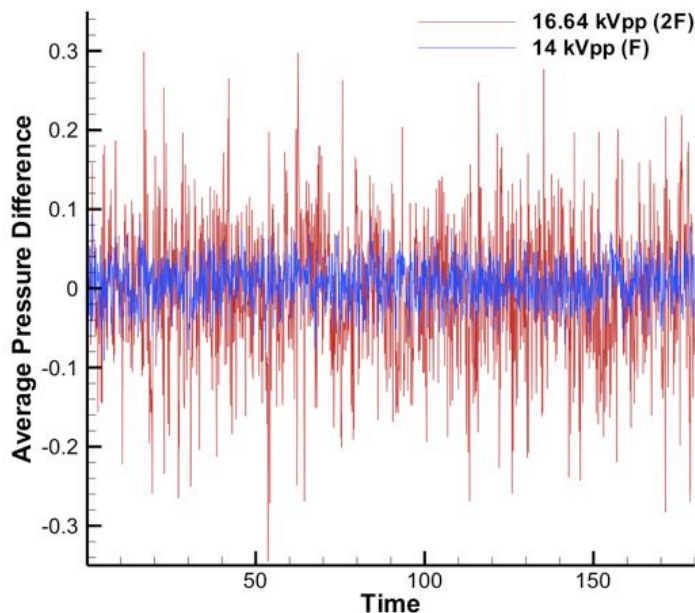


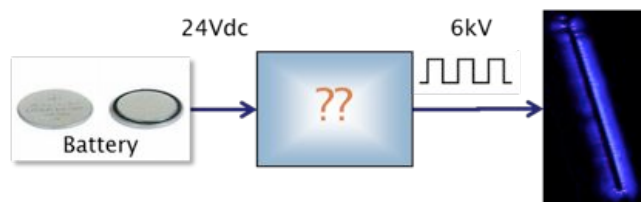**Figure 45. Net pressure force for multiple levels of plasma actuation.**

The nonlinearity in the flight dynamics is indicated by the ratio of response magnitudes to the ratio of excitation magnitudes.  The data in figure 45 is somewhat challenging to immediately analyze due to the high-frequency content; however, the pressures in response to a doubling of the force do not seem to be double those of the initial force. As shown in Table 5, if we calculate the mean and standard deviation of the data in figure 45, we find that the mean pressure for the 16.64 kV case becomes negative with a standard deviation of more than three times that of the 14 kV case.

**Table 5. Mean and standard deviation for the net pressure force.**

| Voltage [kV] | Mean ΔP [Pa] | Standard Deviation [Pa] |
|---|---|---|
| 14 | 0.0064 | 0.0266 |
| 16.64 | -0.0047 | 0.0843 |

## IV.   Novel power supply unit – circuit, simulation and testing.

The WEAV power supply has gone through several evolutions throughout the course of the project. Each achievement aimed to reduce the overall size and weight of the design trying to maintain an optimal voltage output.
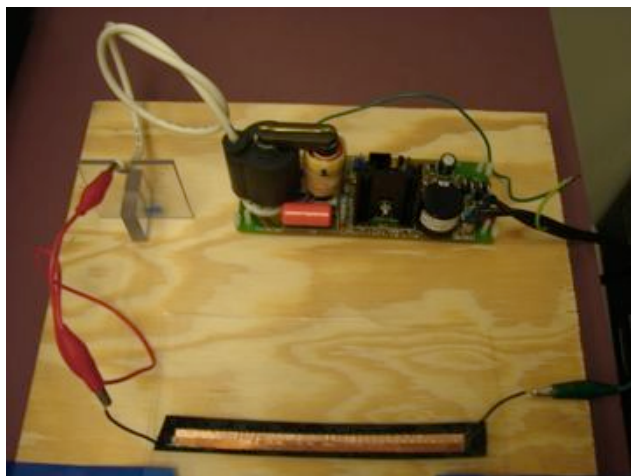
**A. System Considerations**
- *Voltage Output (~kV)*
  - *Power Output (~W)*
  - *Efficiency (> 80%)*
  - *Multiple Channels/Phases*
  - *Load impedance uncertainties*
  - *Mass (10's of g)*
  - *Volume (~ cm$^3$)*

<u>Original Benchtop Power Supply:</u>

The original power supply (**Error! Reference source not found.**) consisted of a function generator, RF amplifier, and a RF transformer. This system was able to generate plasma with a voltage of 14 kv pk-pk. The system total weight was $\simeq$ 26 kg (57 lbs).
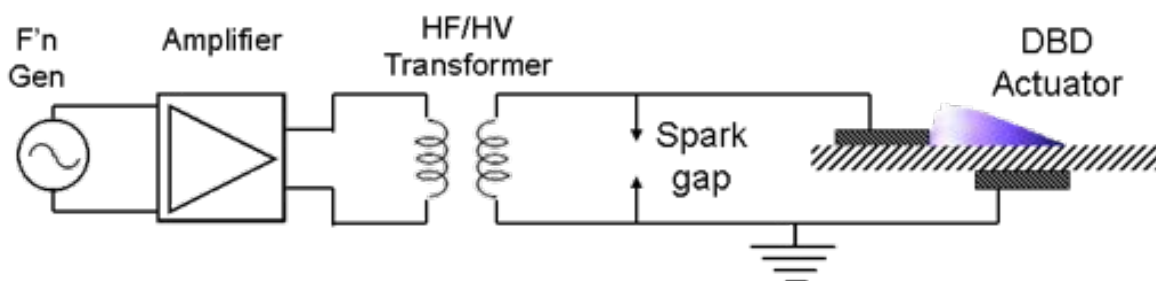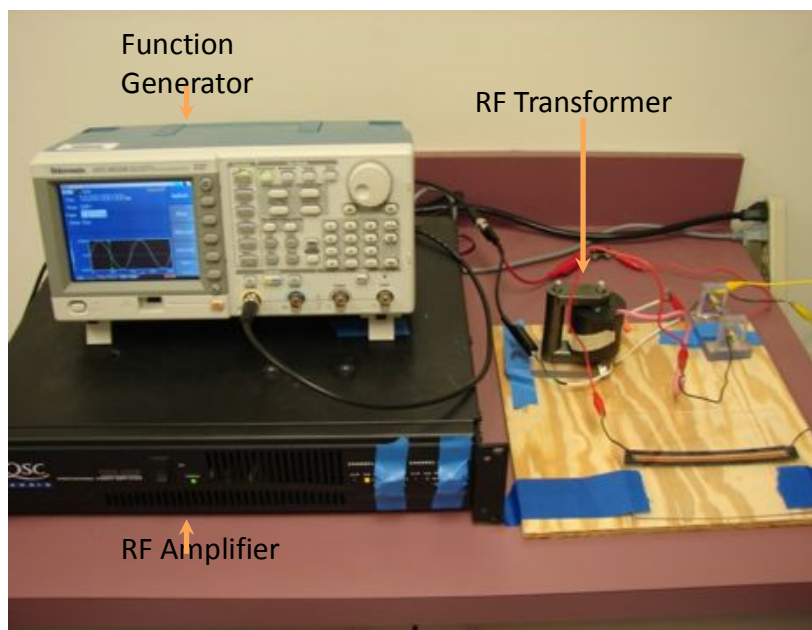




**Figure 29**

*Commercially Available Power Supply:*
- All inclusive circuit contains amplification and frequency modification for plasma generation (Figure 30)
- Still need 120V wall supply
- Total Weight $\simeq$ 340 g
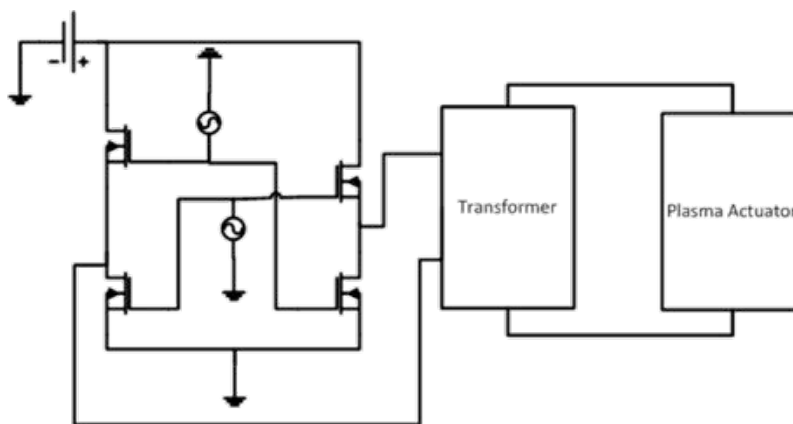
**Figure 30**

Half-Bridge

A half bridge amplifier (Figure 48) enables a voltage to be applied across a load in either direction. The H bridge requires four switches either solid-state or mechanical. The H bridge requires precise control of the switches because only two of the switches should be operated at any given time. If this does not happen then a short circuit will occur.

- Switching circuit producing voltage pulses on the actuator
- Produces voltage square wave into the transformer
- Disadvantage: Requires four transistors , inverter, and a transformer
- Advantage: Allows control of frequency, duty cycle


**Figure 31**

Class D

Class D amplifier (Figure 329) is a switch mode power amplifier.  The basic class D amp consists of a wave generator, switching controller, and a low-pass filter. Class D amplifiers operate using pulse width modulation (PWM).  The input signal is converted into a combination of low and high frequency components.  The high-frequency part of the signal is used to make the wave-form binary so it can be amplified by switching the power devices (transistors). The low frequency portion is the desired signal output.  Once the signal is converted the filter removes the high-frequency components.

- Switched mode power amplifier
- Sinusoidal output
- Disadvantages:
  - Fixed frequency

- • Requires two transistors + inverter
- • Advantages:
  - • No large DC choke (large inductor)
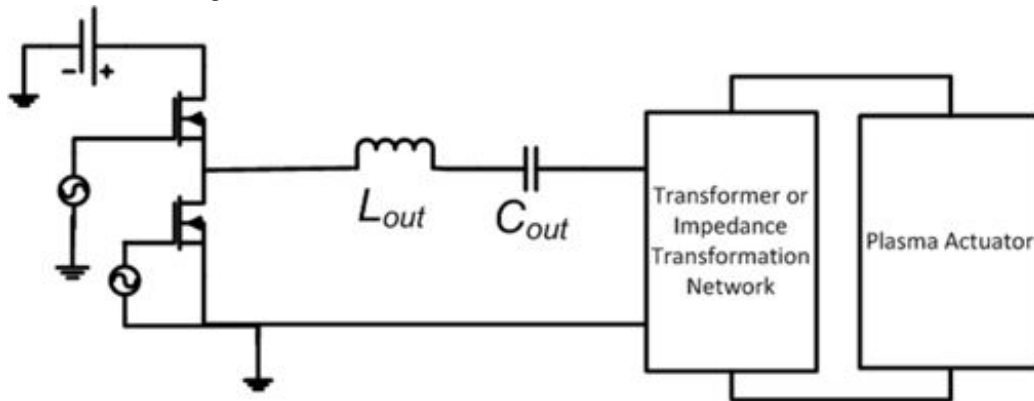  - • Less voltage stress on transistor



**Figure 329**

Class E Amplifier

The class-E amplifier (Figure 330) is a highly efficient switching power amplifier, typically used at such high frequencies that the switching time becomes comparable to the duty time. In the class-E design the transistor is connected via a serial LC circuit to the load, and connected via a large $L_{DC}$ (choke inductor) to the supply voltage. The supply voltage typically is connected to ground via a large capacitor to prevent any RF signals leaking into the supply. The class-E amplifier adds a $C_t$ (capacitor) between the transistors and uses a transformer/impedance matching network to step up the input voltage.

- • Switched mode power amplifier
- • Sinusoidal output
- • Advantage: Only one transistor required and has less components overall
- • Disadvantages:
  - • Fixed frequency
  - • Requires DC choke, $L_{DC}$
  - • Greater voltage stress on transistor (~2.5x that of Class D)
  - • Needs a transformer to step up the input voltage
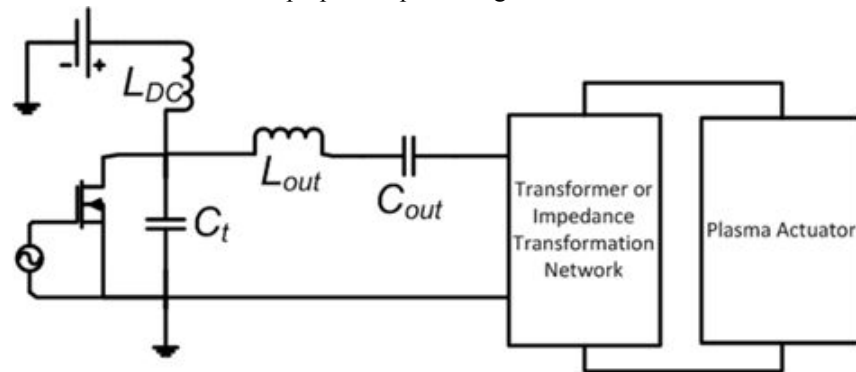


**Figure 330**

Plasma Power Supply

A custom plasma power supply (Figure ) was built based on the class-E architecture. It has a possible voltage output of 15k pk-pk with no load. The custom supply is able to be run in parallel to achieve the same output voltage but with lower power consumption and less stress on the devices. This comes at a cost of 2x the design weight. The single supply has a weight of 54g but requires added driving circuit of about 20 grams.

- Able to generate 8Kv pk-pk (Figure 34)
- Works  off two 9V batteries
- Dimensions 8x4cm
- Variable frequency 30-100KHz
- Power consumption about 13W
- Weight=54g

Dual Plasma Power Supply
- Generates  2x the voltage of single circuit
- Puts less strain on devices
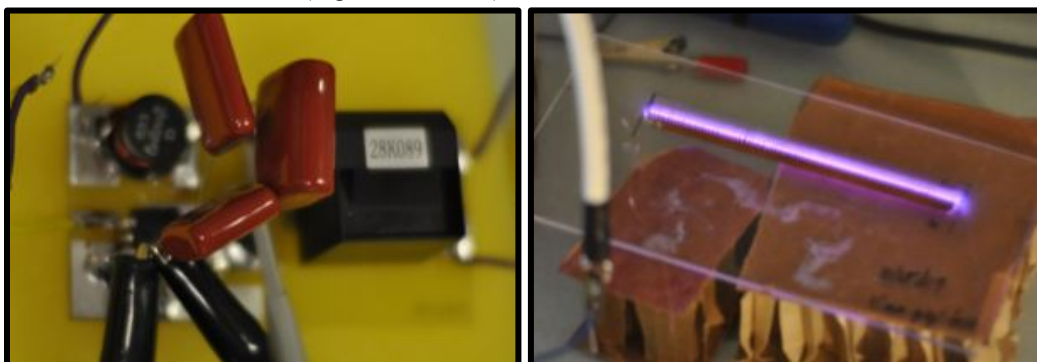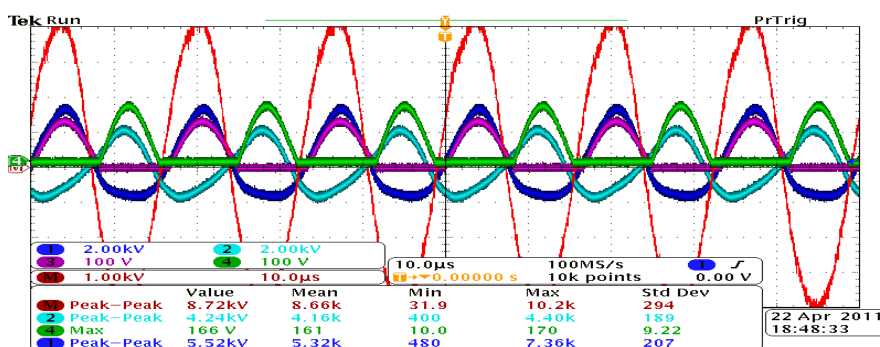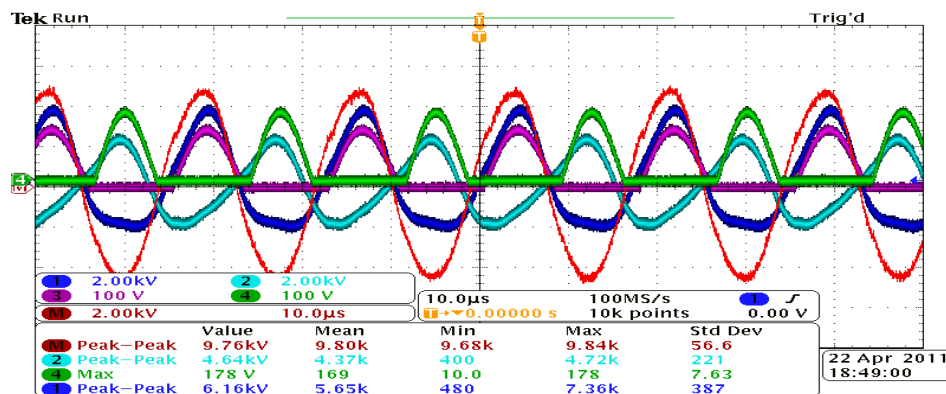- Generated 9.76 kV (Figure 35 and 53)
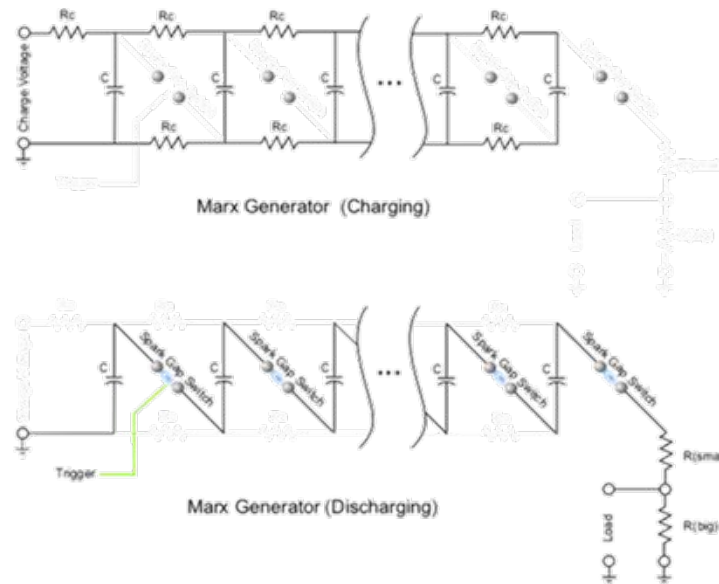


**Figure 51**



**Figure 34**



**Figure 35**

**Marx Generator**



**Figure 54**

The Marx Generator (Figure ) is an electrical circuit composed of capacitors, spark gaps, and resistive elements. Marx generators are used for voltage multiplication. The principle operation of the marx generator is that several capacitors, n, are charged in parallel through resistive elements, R, to the input voltage level, V. The n number capacitors are then connected in series by the spark gaps. The resulting series connection of the capacitors produces an output voltage of n*V at the output. The Marx generator has the highest potential out of the other circuits that have been evaluated. This is because it does not require any magnetic components; therefore it offers the best weight to voltage ratio. Further the Marx can be designed using all active components thus reducing the significant power loss caused by utilizing active elements. With an all active design the marx can be further expanded to an all on chip device. Meaning the marx can be created using a silicon fabrication device drastically reducing the area and weight of the device.

- Switching circuit producing voltage pulse
- N capacitors charged in parallel to voltage V
- Switched by spark gap
- Output is N*V
- Advantage: Requires no heavy magnetic components (inductors and transformer))
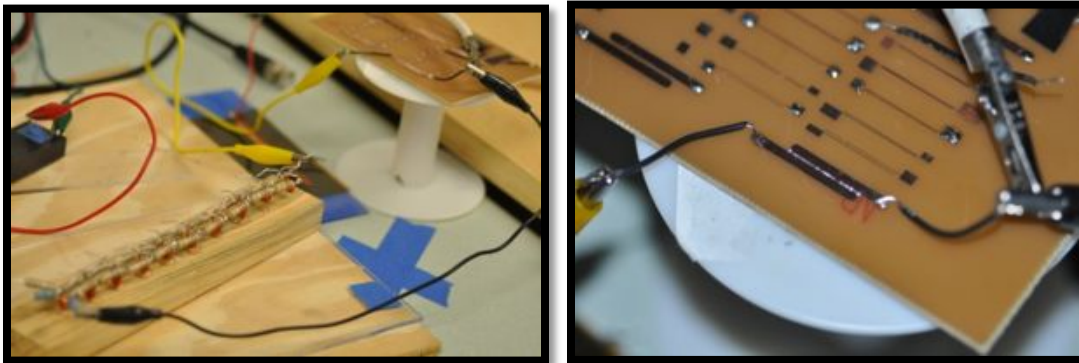- Disadvantage: Best for DC or low-frequency plasma



**Figure 36**

The first marx design that was created was an RC marx (Figure 36) that utilized all passive components and spark gaps as the switching mechanism. This circuit was able to generate a DC like plasma at around 9Kv. This design however was unable to generate DBD plasma due to its low operating frequency of around a few hertz.

- Benefits
  - No bulky transistors
  - No need for extra clock circuitry
  - Current weight=26.8g
- Issues
  - Control of timing with proper spark gap sizing
  - Possible EMI issues with spark gap discharge
  - Low operation frequency

The next phase in the marx generator testing involved finding a suitable replacement for the spark gaps. Electromechanical relays were found as a suitable spark gap replacement. These relays would allow kilohertz operation of the marx generator. A 5-stage Marx generator was designed using the relays. (Figure 37)

- Currently able to generate 8kv with 5 stages ( No Load)
- 5.6Kv with load connected
- Weight= 17.34g
- Clock circuit was unable to drive multiple loads so reached a max amount of stages, 5, after which adding more stages would not increase output voltage.
- Added gate driving circuit for each stage
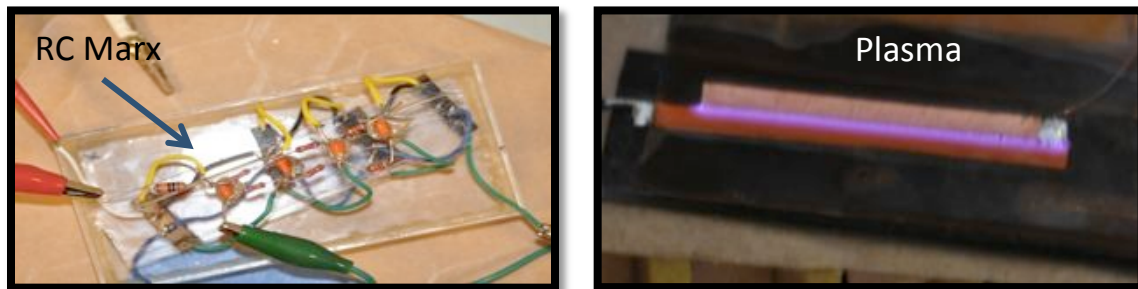  - Added weight of each new circuit=4g



**Figure 37**

The relay marx generator was successfully able to generate DBD plasma (Figure 38). It was also able to generate plasma on a WEAV prototype. However, lift-off was not achieved. Force testing was done on the marx generator and it was determined that the force being generated was approximately <1mg. The required force for lift-off needs to be on the order of grams. A draw back of the relay marx was that it required a large DC-DC converter for the input. The DC converter block weighed 100g which puts the overall system weight to around 117.34 grams. The DC converter block was replaced by a smaller version weighing approximately 38.2g.
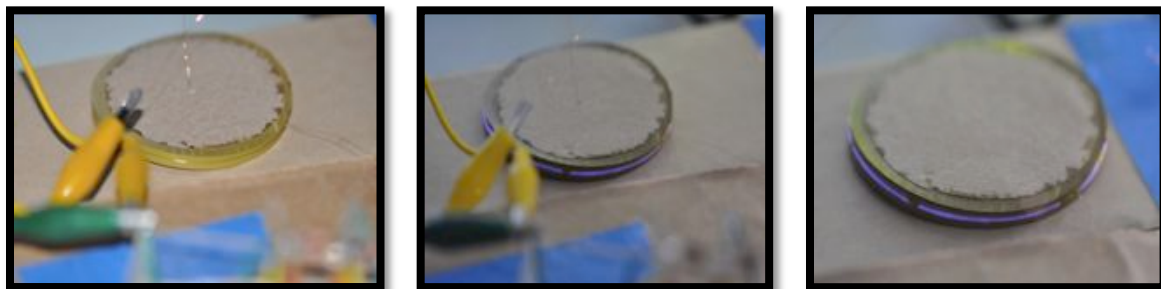


**Figure 38**

The force generated has a frequency dependence; the higher the frequency the higher the force that is generated. The relays were frequency limited to a maximum of 1.2 kilohertz, however for strong plasma generation the frequency needs to be on the order of tens of kilohertz.  At this stage transistors would be the only suitable replacement as the switching device for the marx. There are two possible choices for use as transistors, IGBTs or MOSFETs. (Figure 39)
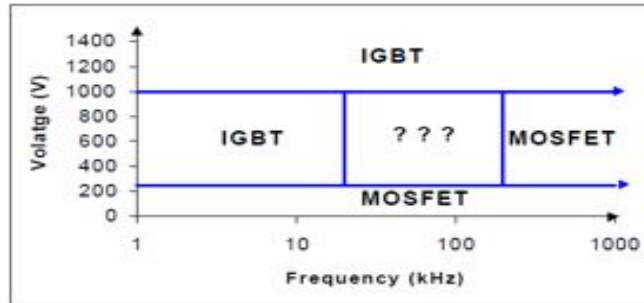
**Figure 39**

- IGBTs are better choice under the following conditions:
  – Low duty cycle
  – Low frequency (<20kHz)
  – Narrow or small line or load variations
  – High-voltage applications (>1000V)
  – Operation at high junction temperature is allowed (>100°C)
  – >5kW output power

After comparing the two transistor choices it was decided that IGBTs were the better design choice since they were more suited for high voltage applications and operated best suited in the desired frequency range. A marx generator circuit was designed using all active components consisting of IGBTs and diodes, but for passive stage capacitance.
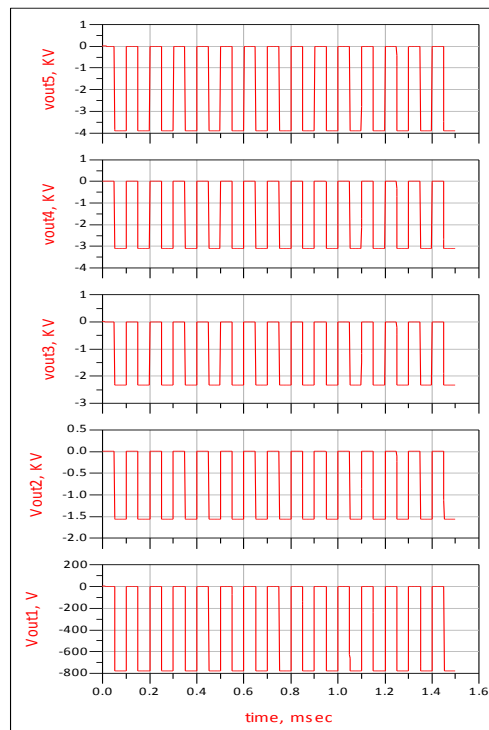
**Figure 59**

A 5-stage marx generator was designed and simulated, using igbt as the switching device. With an input of 800V the circuit was able to generate an output of 3.8KV (Figure ). The expected output for the designed circuit is 4kv, this shows that the proposed design is >90% efficient.

The next step is to build the circuit to verify the simulations. If successful this design has the advantage of the frequency can be increased or decreased if needed without major changes to the overall design. Also for future purposes most of the design can be integrated on an IC making it the most compact, and light weight solution.

## V.  WEAV manufacturing

Introduction

Within the WEAV program, one significant challenge is manufacturing the vehicle itself, which must include a support structure for its own weight and eventual payloads, as well as the electrodes used to produce the vehicle thrust. Requirements include:

- repeatable geometry and performance, including the support structure geometry and electrode placement
- low weight
- adequate structural rigidity
- scalability to larger volume manufacturing.

Acrylic structures

The initial material selected was acrylic. This offered a reasonable compromise between density, electrical properties, and cost. To machine the thin walled parts required to achieve low vehicle weight, a vacuum chuck was constructed to hold the material during the milling process. A photograph of the vacuum chuck is shown in Fig. 60.
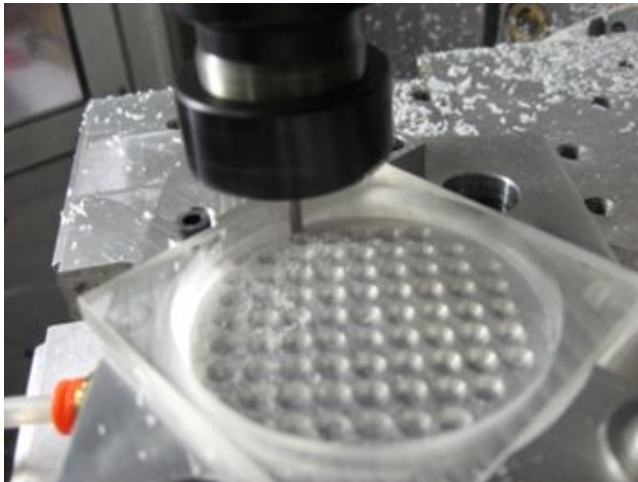


Figure 60: Vacuum chuck with acrylic workpiece.

Due to the heat generated by the current flow through the electrodes (i.e., resistive heating), the acrylic vehicles tended to warp after a short period of time (thermal distortion). Therefore, new designs were considered where ribs were added to stiffen the structure, while minimizing the added weight. An example is shown in Fig. 61. This design weighted 1.0 g, had a base thickness of 0.05 mm bottom thickness with a 7 mm x 0.3 mm side wall. Initial lift was observed, but the part warped and the dielectric failed under high voltages.

Figure 61: Example acrylic vehicle structure with stiffening ribs.

Torlon structures

It was determined that the acrylic material should be replaced with one that did not offer the same sensitivity to resistive heating. Candidate materials included silicon rubber, PMMA, PEEK, and Torlon. Due to its higher thermal conductivity and good dielectric strength Torlon 4203 was selected. A number of design alternatives were pursued to increase the effective length of the electrodes and, subsequently, increase the available thrust. Figure 62 shows an example design, which was machined from a Torlon plate. The limitation imposed by the change in geometry is that the small radii tended to produce failure points on the electrodes.



Figure 62: Torlon 4203 design example.

Hysol molding

A molding procedure was also investigated to enable vehicle structures to be produced from materials that were not well suited to machining. Hysol ES1902 epoxy was selected as a new potential dielectric due to its high dielectric strength (nearly three times that of Torlon). To produce the required thin walled structures, an expendable mold manufacturing process was adopted. First, a wax mold was produced; see Fig. 63. Next, the mold was filled and assembled; see Fig. 64. Vacuum was used to eliminate air bubbles. Finally, the wax was removed using a glycol bath. See Fig. 65. The unexpected limitation for this approach was that the "bulk" dielectric strength suggested by the material manufacturer was not observed for the thin walled components (it was much lower).

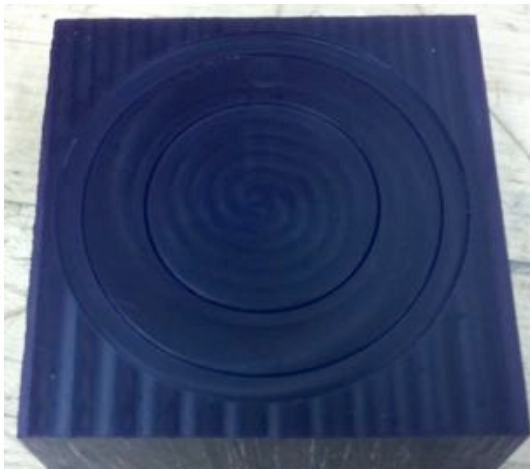Figure 63: Wax mold for hysol molding process.



Figure 64: Assembled mold.



Figure 65: Glycol bath used to remove mold material from hysol vehicle structure.

Silicone rubber
Because silicone rubber was shown to exhibit the dielectric/thermal properties required for the WEAV vehicle, but was not machinable, a hybrid strategy was proposed. In this case, a thin acrylic support was combined with a silicone rubber dielectric barrier for the electrodes. An example is shown in Fig. 66, where a silicone rubber ring is supported by a machined, light weight acrylic skeleton.
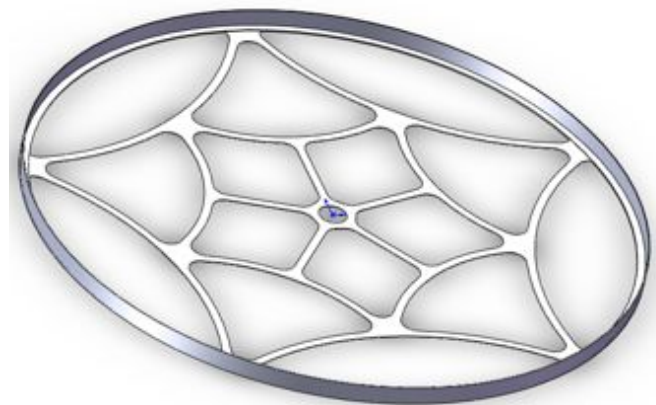


Figure 66: Hybrid silicone rubber (ring)/acrylic (skeleton) design.

To this point, it had been assumed that the available thrust scaled with the third power of the voltage applied to the vehicle electrodes. Therefore, the group had been searching for a material that could withstand the voltage level required to offset the vehicle weight. However, extended testing revealed a "saturation" effect, where the available thrust no longer scaled with the anticipated third power at high (tens of kV) voltages. Given this limit, it was decided that the material densities that were considered reasonable (given acceptable dielectric strength) would not yield a vehicle with a low enough weight to achieve reliable liftoff.

Aerogel
In order to obtain a dramatic decrease in density, aerogels were considered as the vehicle material. They offer low density and high resistance to electrical breakdown. However, they are also brittle, cannot be machined using traditional techniques, and are challenging to manufacturing in bulk form. See Fig. 67.
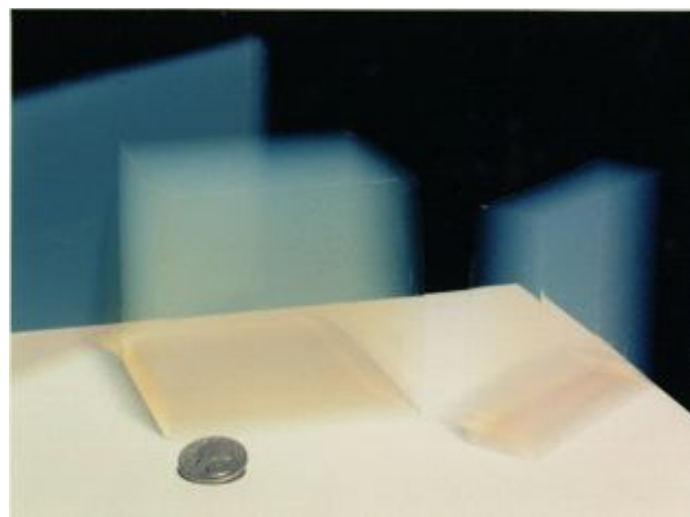


Figure 67: Aerogel examples (http://p25ext.lanl.gov/~hubert/aerogel/).

In order to produce the required structural geometries from the bulk aerogels, picosecond laser micromachining was used. The laser machining setup is shown in Fig. 68. In this figure, the aerogel (light blue component) is located beneath the laser source on a positioning stage.
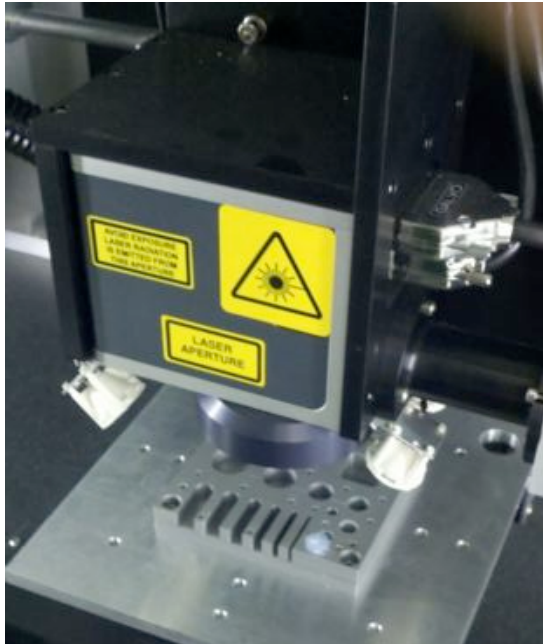


Figure 68: Laser micromachining setup.

A demonstration of the ablation of the aerogel to produce features of the required geometry is provided in Fig. 69. Here, rings with diameters of 1.05 mm, 1.00 mm, and 0.90 mm were machined. A remaining challenge is attaching the electrodes to the aerogel. Testing continues with a focus on heat-sensitive adhesives.
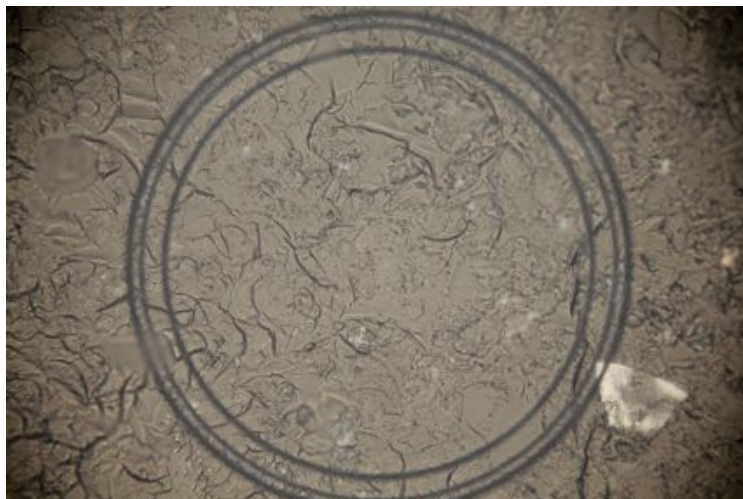


Figure 69: Machined circles in bulk aerogel.

## VI.  Experimental data collection and numerical modeling of a plasma tunnel.

### A.  Introduction

For the WEAV to properly lift off, there must be a sufficient level of thrust due to the effects of a plasma base body force or pressure differential to overcome the effects of the device's weight. The purpose of the 'plasma tunnel' concept is to provide a test bed for which to directly or indirectly measure the effects of the plasma body force and pressure differential. To study these effects more fundamentally, pressure and velocity data was taken from arrays of plasma actuators from two distinct configurations, each of which corresponds to a potential configuration of or portion of an eventual WEAV.

### B.  Open Tunnel

The open tunnel design shown in figure 70 was tested in order to examine some of the expected velocities when a large number of plasma actuators were operated together, similar to what would be expected on some of the large surfaces on the WEAV.

### 1.  Velocity Data

Velocity data was collected downstream of the plasma actuators in an effort to examine their collected effect on producing a sufficiently strong jet of fluid. The plasma devices were constructed on a 2mm thick piece of PMMA, 15cm long by 15 cm wide. The powered electrodes for this device were 2mm wide, and the grounded electrodes were 5mm wide. There was a spacing of 25 mm from the front of one actuator to the front of the next. The first actuator was placed 25mm back from the front of the plate.
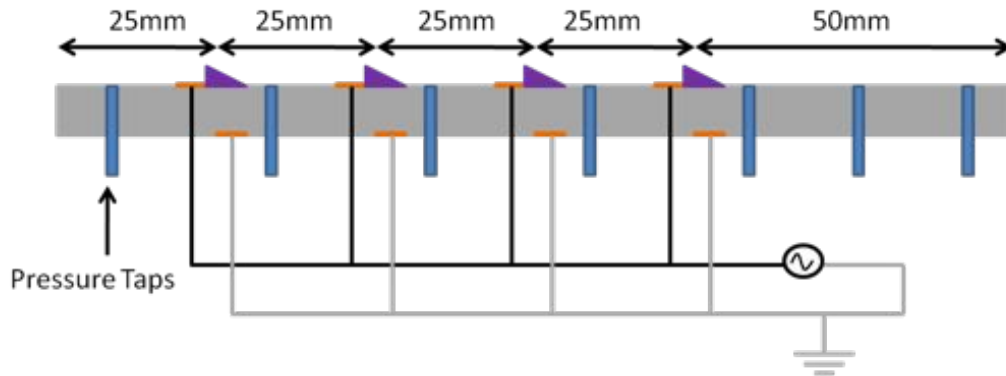


Figure 70 – Schematic of the DBD open tunnel

The wall jet produced by the plasma actuators continued over the remainder of the plate to its trailing edge, with the maximum velocity induced by the plate increasing as the number of actuators and the applied voltage are increased. The momentum addition also increases as these two variables are increased, which indicates that the body force is increasing. There also appear to be decreasing marginal returns as the number of actuators is increased, but a power law relationship as the voltage is increased. That a power law relationship appears to exist is not unsurprising, as this type of relationship has been seen in other thrust and power consumption experiments.
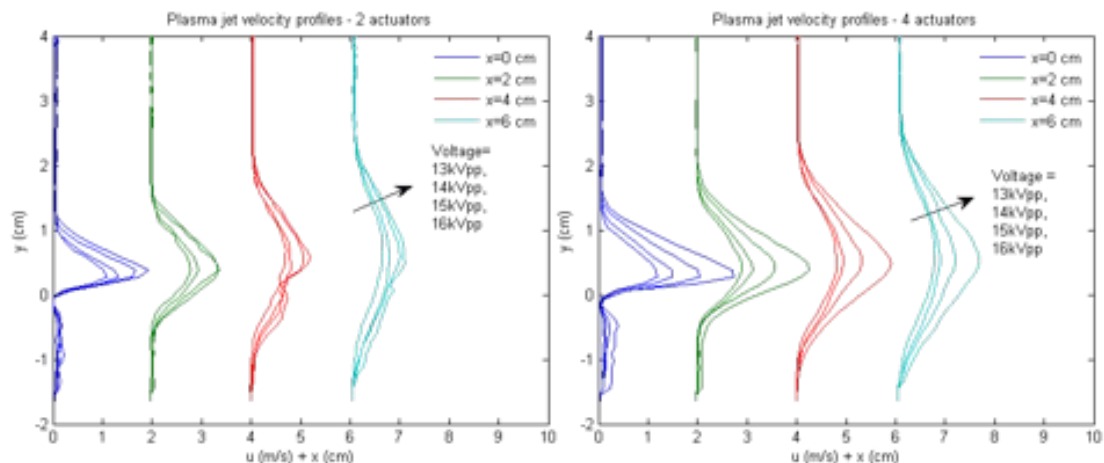
Figure 71 – Wall jet profiles for 2 actuators (left) and 4 actuators (right) as a function of the applied voltage at various positions in space with an applied voltage of 14kHz.
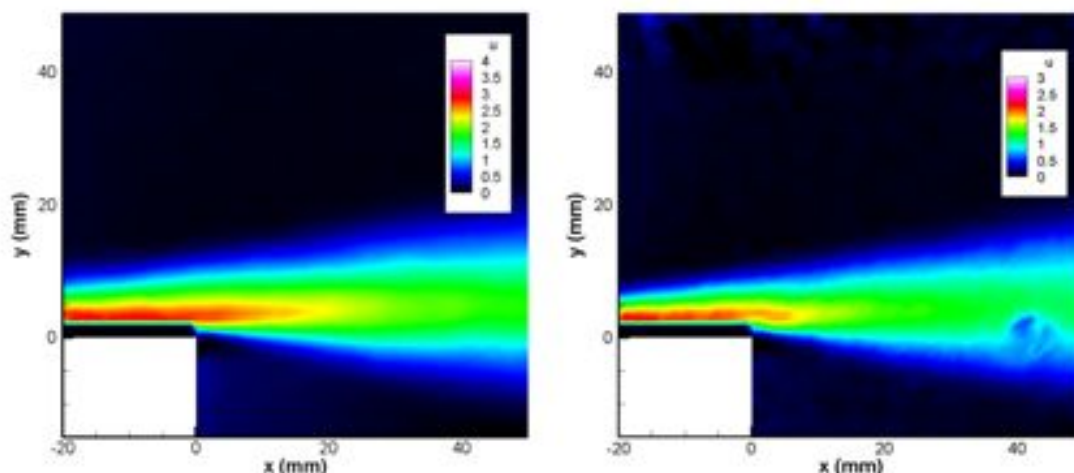


Figure 72 – Flow fields for 2 actuators (left) and 4 actuators (right) at 16kVpp.

### C. Closed Tunnel

A number of plasma tunnels were constructed using 2mm thick PMMA (Plexiglas). The tunnels were constructed with a height of 20 mm. Four actuators were built into each tunnel, located at x=25, 50, 75, and 100mm from the inlet of the tunnel. Pressure taps were located at various points on the sides and upper surface of the tunnel to collect pressure data. PIV data was collected near the exit. A schematic of the set up can be seen in Figure 73.
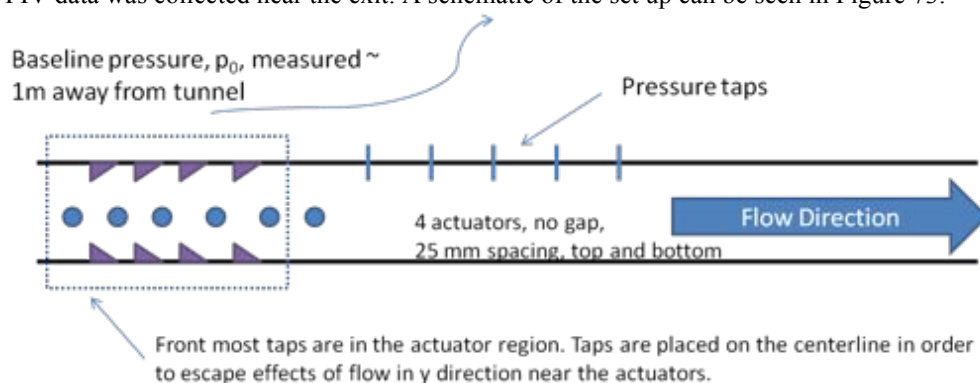


Figure 73 – Schematic of the closed tunnel

### A. Pressure Data

Data collected shows that there is a distinct shape to the surface pressure distribution inside of the closed tunnel. The actuators were constructed using 4mm wide electrodes for the powered and grounded electrodes, with no gap between the rear of the powered electrode and the front of the grounded electrode. The closed tunnels show that across each actuator, the pressure jumps. Directly downstream of the actuators, the pressure continues to rise, indicative of the still developing flow field. Further downstream, where the flow is more or less developed, the pressure slowly drops, balancing any viscous effects. These results can be seen for 1-3 actuators in Figure 74 below. This test was also performed with a screen in place downstream of the plasma actuators; however, the screen presented itself as such a large impedance to the flow, that it prevented a appreciable flow from passing through the tunnel and reduced the effectiveness to unacceptably low levels.

The effects of frequency on the pressure differential were also measured, examining the effects at 10, 14,15 and 20 kHz at 15 $kV_{pp}$ using a single actuator. The results of these tests show a roughly linear relationship between the frequency and maximum pressure differential, which can be seen in Figure 75 below.

This test was also repeated using MBPA devices. These devices were tested, as it was thought that additional performance could be obtained. The specific configuration of the devices was of 4mm wide electrodes with no gap between the rear and front of two adjacent electrodes. The devices did provide some additional benefit (~30% higher pressure differential, Figure 76), but the range of voltages that could be tested was very limited. Due to the thickness of the dielectric, the MBPAs would not produce sufficiently uniform plasma until the voltage was raised to 12kVpp. However, at voltages higher than this, the devices began to discharge to each other, which is a non-ideal effect.
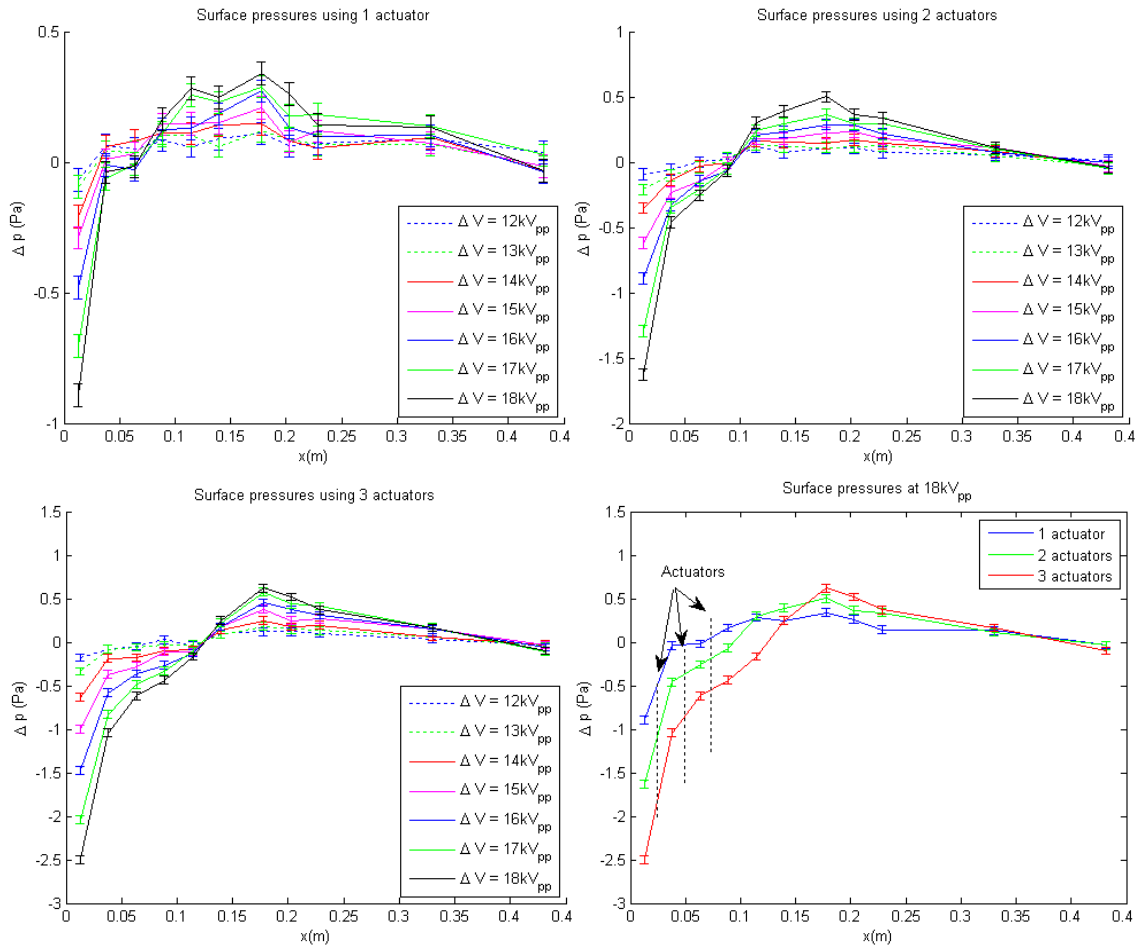


Figure 74 – Surface pressure inside the closed plasma tunnel for 1(top, left), 2(top, right) and 3(bottom, left) actuators as a function of voltage at 14kHz. Data for all three at 18kV$_{pp}$ is also shown (bottom right).
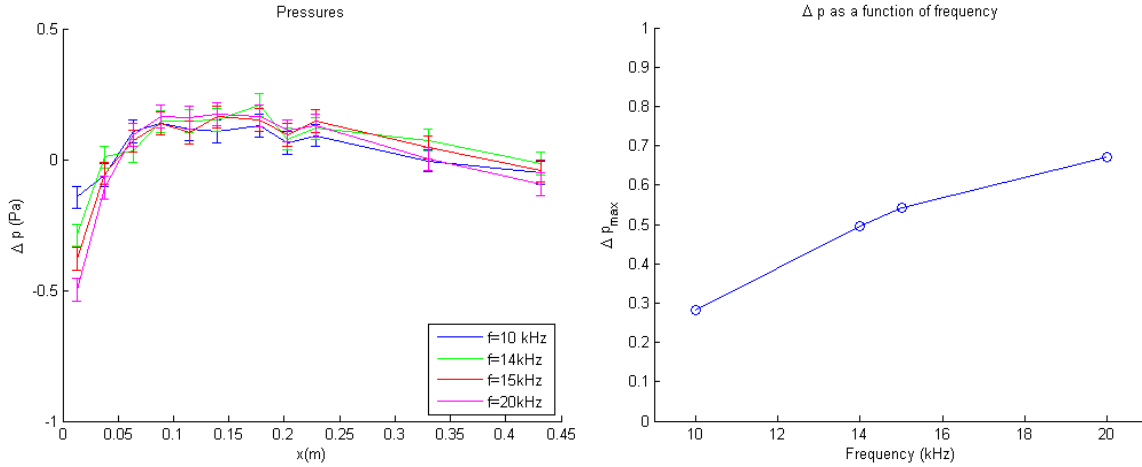
Figure 75 – Surface pressures (left) and maximum pressure differential (right) as function of applied frequency at $15kV_{pp}$ for a single actuator.
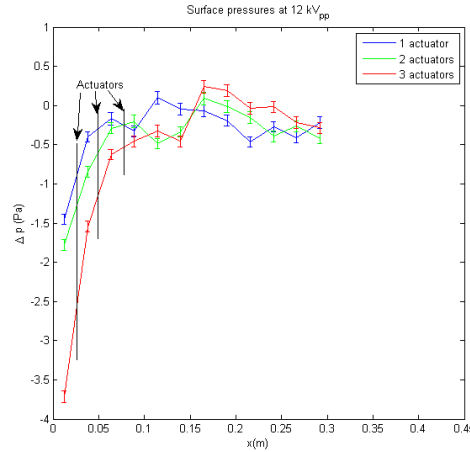


Figure 76 – Measured pressure for the case of using MBPA plasma actuators in the tunnel at $12kV_{pp}$ and an applied frequency of 14kHz.

## B. Functional Relationship

From the complete set of test data collected, functional relationships were able to be created. It was found that the maximum pressure differential ($\Delta p_{max} = p_{max} - p_{min}$) roughly follows a power law relationship with the voltage. A linear relationship with frequency was found earlier, which leads to an approximation of the pressure differential as

$$\Delta p_{max} = Cf(\Delta V)^{5.5} \qquad (5)$$

where C is a parameter based on the geometry of the devices, f is the frequency and Dp is the applied voltage in $kV_{pp}$. For our data with the 4mm wide powered electrode, zero gap, 4 mm wide grounded electrode and 2mm thick PMMA dielectric, we estimate that $C = 3.3E\text{-}8$ Pa $kHz^{-1}kV_{pp}^{-5.5}$.
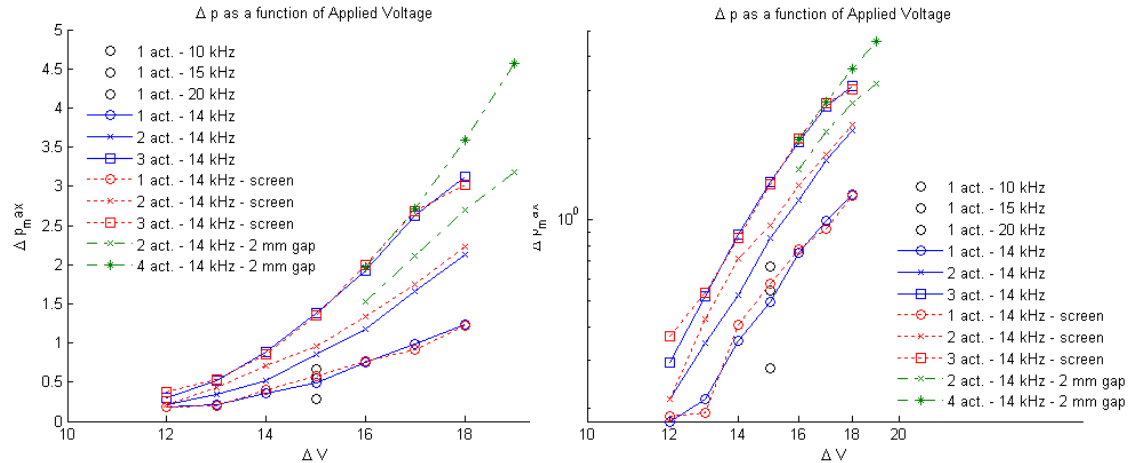
Figure 77 – Collected maximum pressure differential for all of the tests run. Plotted on a linear graph (left) and a log-log graph (right).

## C. Velocity Data

Particle Image Velocimetry (PIV) data was collected at the tunnel exit, including some of the area inside of the tunnel itself. The plasma tunnel appears to create an unsteady, turbulent jet that diffuses out as it moves downstream. This jet does not show any of the wall jet like features that are normally associated with plasma actuators, as the flow exiting the tunnel is sufficiently well developed that those features have decayed away. It can be seen in Figure 78 that increasing the voltage and increasing the number of actuators both increase the maximum velocities experienced in the flow, with the flow velocities ranging from a low of 1 to a maximum of 2.5 m/s. This is lower than that of the 'open' tunnel experiments performed earlier, however, the total volume of fluid in motion is larger due to additional length for the flow to develop in the closed tunnel design. However, there is a diminishing margin of return as the number of actuators is increased. This can be seen in Figure 78. Time mean flow fields of the plasma induced jet exiting the tunnel can be seen in Figure 79.
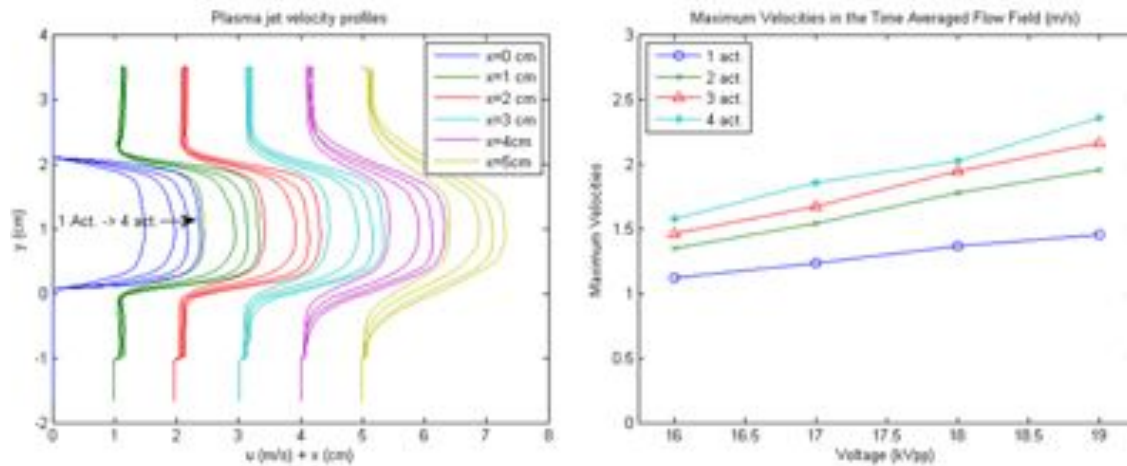


Figure 78 – Jet velocity profiles for 1 to 4 actuators at $19kV_{pp}$ and 14kHz (left) and maximum velocities across a range of voltages and number of actuators (right).
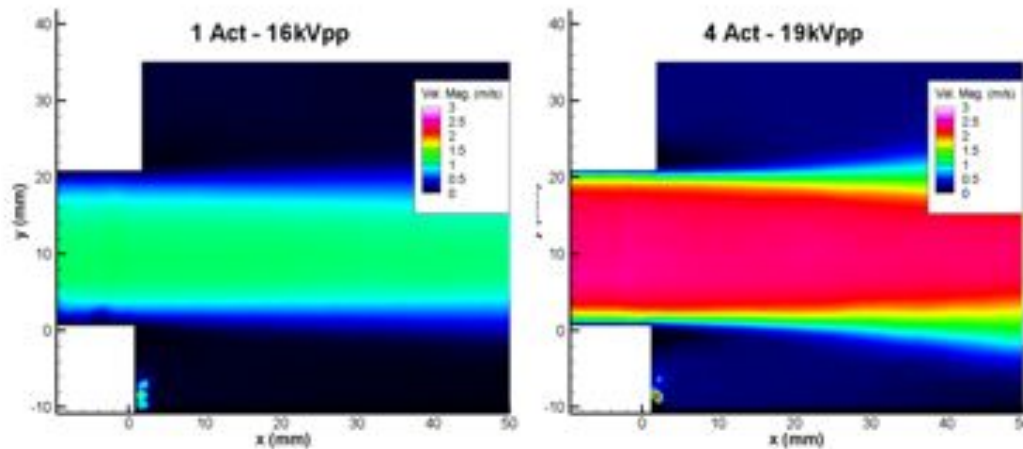
Figure 79 – Time averaged flow field at two different conditions.

Tests were performed in order to examine the flow structure inside of the tunnel. However, various wires, solder, and the adhesives used to construct the tunnel obstructed the view of the camera used as part of the PIV system and prevented the collection of any useful data.

## D. Computational Results

The closed plasma tunnel was also examined using the Air Force Research Lab's (AFRL) Computational Fluid Dynamics (CFD) code FDL3DI. This is a high accuracy CFD code that takes advantage of Implicit Large Eddy Simulation (ILES) methods to simulate what could be very complex flow fields. The computations were performed on a 721x81x51 mesh for 3D simulations, figure 80. The dimensions of the tunnel were taken to be 300 mm long, 20 mm high, and 60 mm wide. No slip boundary conditions were applied for the top and bottom of the tunnel. Periodic boundary conditions were applied in the span wise direction. No shear boundary conditions were applied outside of the tunnel region, with the boundaries extending 250 mm away in order to allow for the appropriate jet exiting the tunnel to form. Plasma actuators were placed at locations 25, 50, 75 and 100 mm from the leading edge, mimicking the experiments performed. The plasma was modeled using the reduced order model developed by Singh and Roy[13]. Simulations were performed for a range of body force magnitudes (combining the effects of frequency and voltage) and number of actuators in the tunnel. These flows are entirely laminar in behavior due to a lack of external disturbance to cause transition and turbulence to occur.
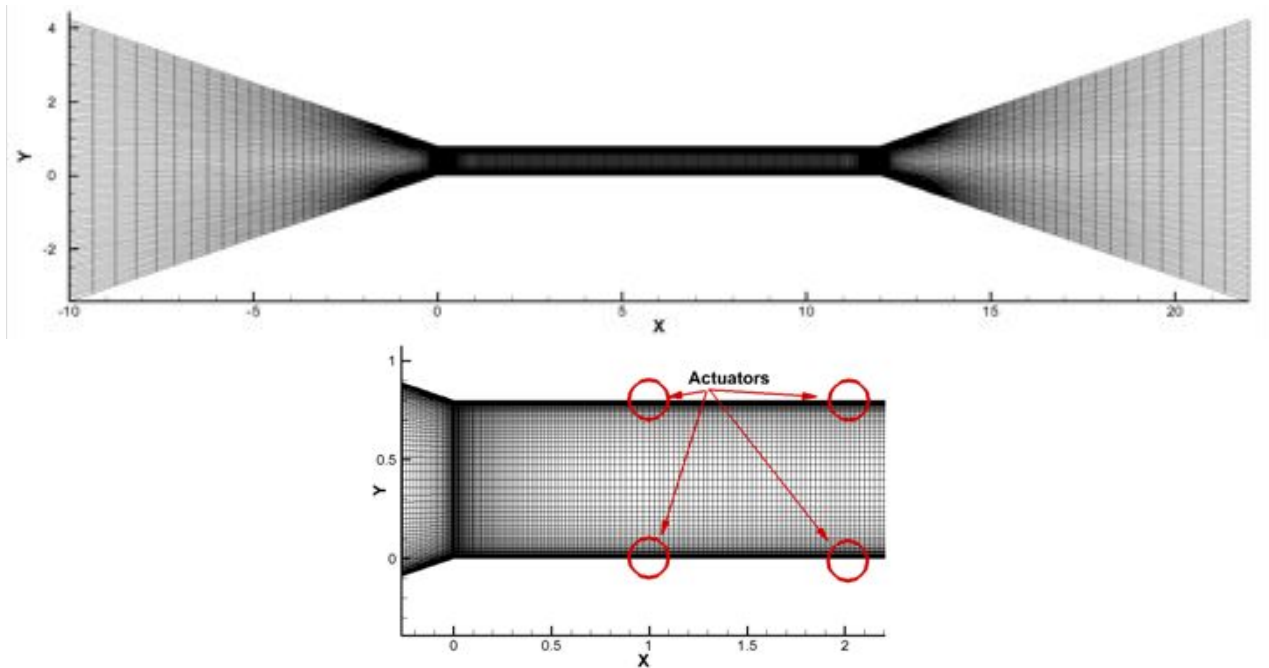
Figure 80 – 2D slice of the computational grid used for the simulations. The full mesh (top) and the region near the first and second sets of plasma actuator (bottom) are shown. 1 unit in space equals 25mm.

In these simulations, the formation and development of the wall jet can be clearly seen. Flow is pulled into the tunnel by the plasma actuators. Directly upstream of the actuators, it is entrained into the wall jet. This wall jet then grows as it moves downstream, with the velocity of the jet decreasing due to the widening nature of the jet. The wall jets also converge and viscous effects begin to take over. As the jet reaches the tunnel exit, viscous effects have pushed the flow to become essential fully developed, which can be seen in Figure 81 below.

As the number of actuators is increased, more of the fluid is entrained into the wall jet farther downstream, allowing for higher velocities, but less length for the flow to develop. With an increased number of actuators, it appears that the flows do not become very well developed, which is in contrast to the experimental results. However, it should be notices that there is no turbulence model or method of transitioning the flow from laminar to turbulent included in these simulations, as such these results only compromise the potentially unstable laminar flow from which a turbulent flow would arise from.
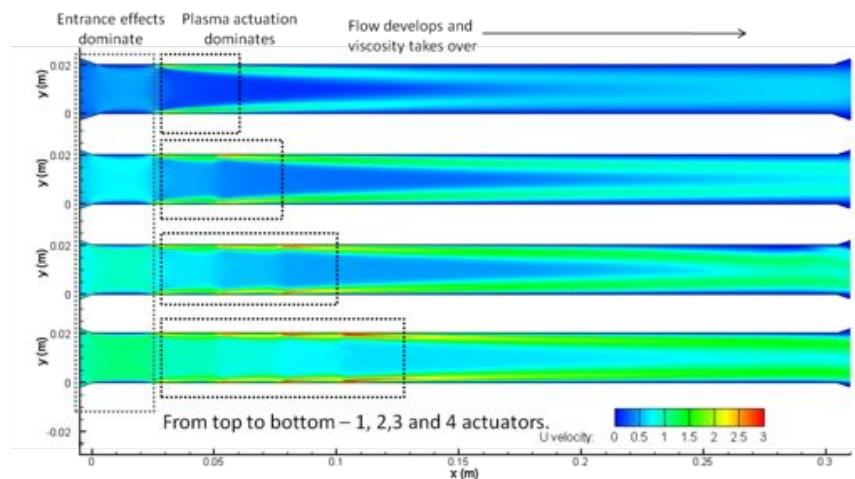


Figure 81 – Flow structure inside of the plasma tunnel for a varying number of actuators. 1, 2, 3 and 4 actuators (top to bottom), placed at x=25, 50, 75, and 100 mm from the leading edge of the tunnel.

Centerline pressure data was also collected (Figure 82). It can be seen that this data quantitatively matches up with that of the 14kVpp case shown above. This data shows that there is a sudden drop in pressure at the inlet of the tunnel, with abrupt increases in the pressure across each actuator. As the flow develops, the pressure rises and then falls again, returning to the free stream pressure at the exit.
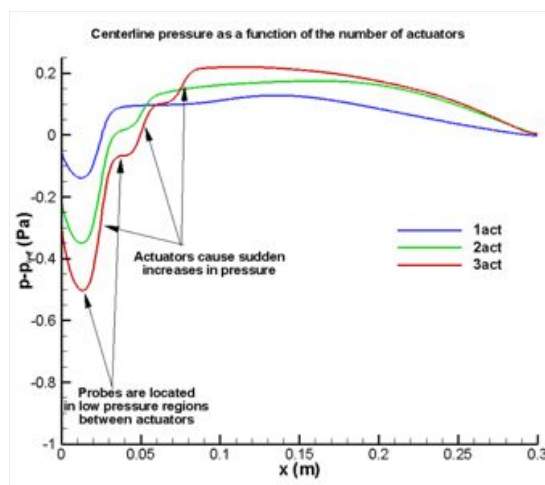


Figure 82 – Centerline pressure in the plasma tunnel for a varying number of plasma actuators.

The magnitude of the body force was varied over half an order or magnitude, roughly corresponding to what would be physically reasonable. The effects of the wall jet became amplified as the strength of the actuation increased, and the flow required more and more tunnel length to become fully developed. However, it is expected that transition would occur, which was not seen in the simulations due to a lack of an external disturbance to begin the transition process. As such, no additional physical processes apart from what was seen above were found.

No slip/symmetric boundary conditions (finite span) were also tested, with minimal changed to the flow, other than additional boundary layers for the third no slip boundary in the no slip/symmetric case.

## References

[1] R.J. Durscher and S. Roy, 2011, On Multi-Barrier Plasma Actuators, AIAA-2010-958, 49th AIAA Aerospace Sciences Meeting, Orlando, FL.

[2] C.-C. Wang, R. Durscher and S. Roy, 2011, Three-dimensional effects of curved plasma actuators in quiescent air, Journal of Applied Physics, 109, 083305.

[3] Santhanakrishnan A. and Jacob, J., "Flow control with plasma synthetic jet actuators," *J. Phys. D: Applied Physics.*, Vol. 40, 2007

[4] R.J. Durscher and S. Roy, 2011, Induced Flow from Serpentine Plasma Actuators Acting in Quiescent Air, AIAA-2011-957, 49th AIAA Aerospace Sciences Meeting, Orlando, FL.

[5] Wang C.-C. and Roy S., "Microscale Plasma Actuators for Improved Thrust Density," J. Appl. Phys., 106 (2009).

[6] Enloe CL, McLaughlin TE, VanDyken RD, et al., "Mechanisms and Responses of a Single Dielectric Barrier Plasma Actuator: Plasma Morphology", *AIAA J.*, 42, 3, 589-594, 2004.

[7] Zito J, Arnold D, "Fabrication and Electrical Characterization of Microscale Dielectric Barrier Discharge Devices", Solid-State Sensors, Actuators, and Microsystems Workshop (Hilton Head), Hilton Head, SC, pp. 238-241, 06/2010.

[8] Durscher RJ, Roy S, "Force Measurement Techniques and Preliminary Results Using Aerogels and Ferroelectrics for Dielectric Barrier Discharge Actuators", *42nd AIAA Plasmadynamics and Lasers Conference*, Honolulu, Hawaii, June 27-30, 2011.

[9] Hoskinson AR, Hershkowitz N, Ashpis DE, "Force Measurements of Single and Double Barrier DBD Plasma Actuators in Quiescent Air", *J. Phys. D: Appl. Phys.*, 41, 245209, 2008.

[10] Joussot, R., Hong, D., Rabat, H., Boucinha, V., Weber-Rozenbaum, R., and Leroy-Chesneau, A., "Thermal Characterization of a DBD Plasma Actuator: Dielectric Temperature Measurements using Infrared Thermography,"*40th Fluid Dynamics Conference and Exhibit*, AIAA2010-5102, Chicago, IL, 2010.

[11] Thomas, F. O., Corke, T. C., Iqbal, M., Kozlov, A., and Schatzman, D., "Optimization of Dielectric Barrier Discharge Plasma Actuators for Active Aerodynamic Flow Control," AIAA Journal, Vol. 47, No. 9, 2009, pp 2169-2177.

[12] Hrubesh, L.W., Keene, L.E., and Latorre, V. R., "Dielectric properties of aerogels", Journal of Materials Research, Vol. 8, 1993, pp 1763-41.

[13] Singh, K. P., and Roy, S., "Force approximation for a plasma actuator operating in atmospheric air," Journal of Applied Physics, Vol. 103, No. 013305, 2008, pp. 1-6.

[14] Lind, R., Snyder, K. and Brenner, M., "Wavelet Analysis to Characterize Nonlinearities and Predict Limit Cycles of an Aeroelastic System," Mechanical Systems and Signal Processing, Vol. 15, No. 2, 2001, pp. 337-356.